

Radiative lifetime of localized excitons in transition-metal dichalcogenidesSabrine Ayari,^{1,*} Adlen Smiri,^{1,†} Aida Hichri,^{1,‡} Sihem Jaziri,^{1,2,§} and Thierry Amand^{3,||}¹*Faculté des Sciences de Bizerte, Laboratoire de Physique des Matériaux: Structure et Propriétés, Université de Carthage, 7021 Jarzouna, Tunisia*²*Faculté des Sciences de Tunis, Laboratoire de Physique de la Matière Condensée, Département de Physique, Université Tunis el Manar, Campus Universitaire 2092 Tunis, Tunisia*³*Université de Toulouse, INSA-CNRS-UPS, LPCNO, 31077 Toulouse, France*

(Received 24 March 2018; revised manuscript received 3 October 2018; published 30 November 2018)

Disorder derived from defects or local strain in monolayer transition-metal dichalcogenides (TMDs) can lead to a dramatic change in the physical behavior of the interband excitations, producing inhomogeneous spectral broadening and localization leading to radiative lifetime increase. In this study, we have modeled the surface disorder of a monolayer TMD sample through a randomized potential in the layer plane. We show that this model, applied to a monolayer of WSe₂, allows us to simulate the spectra of localized exciton states as well as their radiative lifetime. In this context, we give an in depth study of the influence of the disorder potential parameters on the optical properties of these defects through energies, density of states, oscillator strengths, photoluminescence (PL) spectroscopy, and radiative lifetime at low temperature (4 K). We demonstrate that localized excitons have a longer emission time than free excitons, in the range of tens of picoseconds or more, the radiative decay time depending strongly on the disorder parameter and dielectric environment. Finally, in order to prove the validity of our model, we compare it to available experimental results of the literature.

DOI: [10.1103/PhysRevB.98.205430](https://doi.org/10.1103/PhysRevB.98.205430)**I. INTRODUCTION AND MOTIVATION**

Due to the confinement into a single layer and reduced dielectric screening, the family members of transition-metal dichalcogenides monolayers (MLs-TMDs) are characterized by robust, nonhydrogenic excitonic series with binding energies in the order of hundreds of meV [1–12]. They present strong absorption and short population lifetime, in the picosecond range for excited states close to the gap [13–15]. These features make TMDs attractive materials in electronics [16–18], optoelectronics [19–22], including photodetectors, light-emitting diodes, and, more recently for lasers [23–27], photonic devices [28,29], and, due to their specific band structure, valleytronics [30–32]. For instance, the optical properties of ML tungstenides such as WSe₂ or WS₂ are usually dominated by two direct excitonic transitions (e.g., 1.75 and 1.72 eV in WSe₂), usually identified as excitons and trions, respectively [2,4,6]. At low temperature, excitation power dependence measurements proved the existence of multiple emission peaks in ML TMD flakes, which are located below the neutral and charged exciton peaks [2,4,6,33–46]. The nature of some low-energy lines remains unknown and still under debate [4,6,40–46]. Actually, understanding their

microscopic origin is an outstanding open question ever since their first observation in the PL measurements of ML-WSe₂ by Jones *et al.* [41]. Surprisingly, the nature and the identification of these peaks strongly depend on the experimental conditions such as temperature [6], excitation power [4,40], doping density [47], substrate (gold, SiO₂, or h-BN) [38,48–50], and quality (chemically treated [51], or encapsulated with h-BN [38]), and is related to the sample type, molybdenide or tungstenide (Mo/W) [38,40,47]. In fact, experimental results show that these low-energy peaks appear more systematically in tungstenide (WX₂) materials but they are conspicuously absent in molybdenide families (MoX₂) [38,40,47]. This is likely related to the different ordering of the spin-orbit split conduction bands, already known to have deep consequences on the optical properties of TMD materials. As a fact, the primary difference between MoX₂ and WX₂ families is the value and the sign of the conduction spin-orbit splitting ΔE_{SO} [52–54]. As a consequence, the dipolar band to band transitions with the upper valence band are allowed only with the upper conduction states at *K* and *K'* in tungstenides, while the reverse occurs in molybdenides. As a result, taking also into account the electron-hole exchange contribution [52], dipolar active (bright) excitons lie above dark ones in tungstenides, while the reverse is predicted for molybdenides, with some consequences on the exciton relaxation/recombination dynamics [52–54]. Additionally, it has been proposed that in tungstenides an exciton reservoir in the dark states with long radiative time could develop under optical pumping, which could feed in turn the localized states, while this process could be less efficient in molybdenides since the dark states

*first.sabrineaari8@gmail.com

†Second.smiriadlen4@gmail.com

‡thierd.aidaezzedini@gmail.com

§fourth.sihem.jaziri@fsb.rnu.tn

||fifth.amand@insa-toulouse.fr

lie at higher energies than the bright ones, hence, the radiative recombination of the latter would be more favorable than the energy relaxation towards localized states [53]. These features might be at the origin of the appearance of these peaks in WX_2 but not in MoX_2 .

Apart from bright and dark excitons, we can also distinguish between direct and indirect excitons [47]. A direct exciton is formed from an electron-hole pair where the conduction electron and the lacking valence state are taken within the same valley, which consequently results in a direct-gap optical transition for spin singlet excitons. Indirect excitons, on the other hand, arise if the conduction electron and the lacking valence state are taken in opposite valleys [47]. For indirect optical transitions to occur, the large momentum mismatch of the photons and indirect excitons has to be overcome by external agents such as short-wave phonons. This hypothesis has been investigated in Ref. [48] for $MoSe_2$ and WSe_2 at low temperatures. However, we note that the low-energy lines disappear in the latter compound at temperatures typically above 150 K [6], suggesting a thermally activated delocalization mechanism.

At a low temperature (4 K) and low excitation density, Wang *et al.* [6] and M. Koperski *et al.* [44] recorded an anharmonic emission band (exhibiting a fingerlike pattern) below the free exciton line, in tungstenide materials, which is attributed to the defect-localized excitons. Other authors, like Plechinger *et al.* [40,45,46], have demonstrated that on WS_2 ML, at high excitation density, the biexciton (XX) emission is dominant, while at low excitation density the main contribution to the PL peak stems from defect-bound excitons. Besides, doping leads to profound changes in the photoluminescence or differential reflectance measurements of ML TMDs. In fact, by applying a gate voltage, Jones *et al.* [41] showed in PL experiments on a WSe_2 ML that the spectral weight of PL transfers from the neutral exciton (X_0) to the trion (X_-), and, at a voltage higher than 20 V, they proved the appearance of a new PL feature (named X'_2), positioned at the same energy as the biexciton emission and behaving in the same way as the trion. Thus they suggest that X'_2 probably arises from the fine structure of the trion [40,41]. In the same context, at 20 K, and at high-doping regime ($n \geq 5 \times 10^{12} \text{ cm}^{-2}$), an additional peak develops at low energy in electron-doped WX_2 MLs, having a very strong amplitude in emission experiments [47]. It has been shown theoretically that the qualitative density dependence of this feature, and its absence in Mo-based compounds or hole-doped samples, is actually consistent with the occurrence of an exciton-intervalley (shortwave) plasmon quasiparticle. Besides, direct and indirect excitons can be coupled via intervalley (shortwave) plasmons, in strongly doped samples. These plasmons originate from the short-range Coulomb potential allowing spin conserving electron transitions between valleys [47]. However, at low-doping level (typically $n \leq 10^{12} \text{ cm}^{-2}$), these many-body effects disappear, trions display vanishingly small oscillator strength in reflectivity experiments [55], while a PL line survives in the vicinity of the previous trion lines (although now without any splitting for X_- in WSe_2). Furthermore, it has been proposed recently, for samples on SiO_2 substrate, that this line could be interpreted as a bright-exciton recombination assisted by

optical phonon emission, a second-order process enhanced by the proximity of a localized virtual trion state, which is quasiresonant with the emission energy [56].

In our study motivated by the work of Wang *et al.* [6], we assume that in low-doping density and weak excitation power, these peaks originate in the defects that exist in the monolayer of WSe_2 , which are unintentionally generated during materials synthesis or when transferring a monolayer onto the substrates [57,58]. For instance, chalcogen vacancies may create local strain contributing to spatial potential fluctuations for electrons and holes. Similar effects are observed in WS_2 [13,59]. Here, we aim at modeling and interpreting only the localized bright-exciton light emission in ML TMDs, focusing on the case of WSe_2 deposited on the SiO_2/Si substrate and exposed to the air. Only the orbital states are considered, since we have discarded the electron-hole Coulomb exchange interaction. The latter would lead to a more complex spectrum, accounting for the exciton fine structure. The splitting between bright (spin singlet) and dark (spin triplet) intravalley excitons is basically due to short-range exchange interaction, plus a spin-orbit contribution specific to TMD materials [52]. Note that only “singlet” free excitons within the radiative light cone ($K_\Gamma < \frac{n_{\text{eff}}\omega}{c}$) can recombine emitting photons, so that for localized states, only the component of the exciton wave packet within this cone participate in the oscillator strength. The center of mass exciton localization could, in principle, be possible both for direct bright (where the electron in conduction band has a spin and a valley states identical to that of the electron removed from the valence band) and direct dark excitons (where the electron in the conduction band belongs to the same valley but has a spin state opposite to that of the electron removed from the valence band). However, we restrict ourselves to the case of bright excitons, the only ones allowing a straightforward comparison of our model with experiment. On the other hand, the long-range component of Coulomb exchange acts only in the subspace of direct “singlet” excitons. It splits the transverse and longitudinal free excitons, with a K_Γ -dependent splitting [60]. It does not work for nonoptically active electron-hole pairs, i.e., for spin triplet excitons. For localized excitons, the long-range exchange interaction could manifest by a small splitting of bright states, if the confinement potential has a symmetry lower than the crystal one, as is the case in classical semiconductor quantum dots (for example, for a harmonic well with different curvatures along two orthogonal axes). This relatively weak splitting is neglected in our work, since we consider only orbital states.

Indirect $K(K')$ excitons (where localization implies that both K and K' states participate to the localized state), if spin allowed, can only recombine emitting phonons at low temperature. (In these states, short-range exchange interaction is expected to be weaker than for a direct exciton.) Without any clear experimental evidence of corresponding lines in the emission spectrum, these indirect excitons are not considered here as well.

The large exciton and trion binding energies imply that many-body interactions play an important role in determining the optical properties of these materials at high density or in presence of an electron gas [55,61–64]. For most

optoelectronic applications, knowing the radiative lifetimes of elementary excitations and the parameters that affect this latter is of key importance for realizing applications of these novel materials [6,61–67]. Recent experimental and theoretical studies also demonstrated that the radiative lifetime of the localized exciton is expected to be more sensitive to the sample parameters (substrate material, interface defects, etc.) than the free exciton one [6,62,68]. In fact, since radiative rates of excitons are limited by momentum conservation requirements, localization can enhance or reduce significantly the intrinsic radiative rate of excitons by broadening the distribution of their center of mass momenta [61,62]. It is important to note that in recent experimental results the distinction between “localized” and “delocalized” is blurred by the finite lifetime [6,61]. It is therefore of fundamental importance to understand the effect of disorder and the environment in order to determine the radiative emission processes of localized excitons. In a previous work [69], we had studied the effect of the dielectric environment surrounding the ML-WS₂ on the fundamental properties of exciton and trion using the Rytova-Keldysh potential [70] and we had given a quick discussion on the disorder model [69]. In this work, in contrast to Ref. [69], we provide a systematic study of the dependence of the localized exciton states and their radiative properties not only on the correlation length L but also on the potential fluctuation amplitude V_0 . We study in detail the effect of the disorder parameter on the optical properties of monolayer WSe₂, and we investigate the impact of different dielectric environments, particularly on the radiative lifetime. On a technical point of view, we have also optimized the role of the number of spatial modes necessary to build the potential landscape (here amounting typically to $N = 1000$). In addition, we provide here with details a complete technical description and discussion about the analytical matrix elements calculation using Hermite polynomials, the justification of the choice of the center of mass basis, the relevant parameter range of our model, and the explicit analytical expression for the spatial correlation function arising from the generated disorder. Moreover, a full calculation of the radiative decay time of the localized exciton has been done. All these elements, not developed before, allowed us to make a quantitative fit to the experimentally observed localized exciton line decay times and spectral position on the example of WSe₂ with a single couple of parameters (V_0, L), which definitely improves and generalizes our previous approach in Ref. [69], and validates our model.

The organization of this article is as follows. In Sec. II, we introduce our random potential fluctuation model in order to describe the exciton center of mass localization; we discuss the relevant parameter range for the model and, using the Fermi golden rule, we calculate the radiative lifetime of the localized exciton at low temperature in ML-WSe₂. In Sec. III, in order to provide further insight into the behavior and origin of the excitonic localized states in ML-WSe₂, we discuss the influence of the coherence length of the random disorder potential on the optical properties at $T = 4$ K, namely, the emission energies, probability distributions of excitonic states, and radiative lifetime in different disorder realizations. In Sec. IV, we investigate the influence of the disorder potential fluctuation amplitude. The dielectric environment effect on

the radiative lifetime of the localized excitons at low temperatures in ML-WSe₂ will be studied in Sec. V. In Sec. VI, we compare our results with time-resolved photoluminescence (TRPL) spectroscopy experiments available in the literature. Finally, in the last section, we present our conclusions.

II. FORMULATION OF THE LOCALIZED EXCITON PROBLEM

In our work, we cover a regime of low temperature, low-doping density, and under low-density excitation. According to these conditions, our theory does not capture optical transitions that are associated with trions and their fine structure, biexcitons, excitons (shortwave) plasmon coupling, as well as phonon emission. Our study is focused on bright exciton states, so that we will not consider here the localization of dark states, and more generally the influence of short-range/long-range electron-hole exchange. It aims at understanding the exciton center of mass localization in ML TMD originating from defects, by studying the impact of disorder potential originating from defects on exciton states and radiative lifetime. The model is then compared with experimental data on ML-WSe₂ available in the literature.

In this section, we will present the study of the disorder effect in three steps. In step 1 (Sec. II A), we calculate the eigenstates and eigenvalues of a localized exciton by solving the effective Schrödinger equation. In step 2 (Sec. II B), in order to understand the framework of the disorder potential, we will give a theoretical description of the influence of the disorder parameters on the optical properties. In step 3 (Sec. II C), by using the Fermi golden rules and the oscillator strength evaluated in step 1, we will calculate the radiative lifetime of the localized excitons.

A. Description of the Hamiltonian of the localized exciton via disorder potential

To model the localization of the exciton, we choose the case of a spatially random disorder potential that binds the center of mass of the electron-hole pair. To achieve this, we describe the disorder potential by a Gaussian random field for electrons and holes $V_{e,(h)}(\rho_{e,(h)})$, created from a superposition of N random plane waves with random direction θ_i , random phase ϕ_i , and a wavelength L , which will be shown later to correspond to the disorder potential correlation length

$$V_{e,(h)}(\rho_{e,(h)}) = \frac{V_{0;e,(h)}}{\sqrt{2N}} \sum_{i=1}^N \text{Re}\{e^{i(\mathbf{K}_i \cdot \rho_{e,(h)} + \phi_i)}\} \quad (1)$$

with $\mathbf{K}_i = (\frac{2\pi}{L} \cos \theta_i, \frac{2\pi}{L} \sin \theta_i)$, ρ_e and ρ_h are the in-plane position vectors for the electron and the hole, respectively, $V_{0;e,(h)}$ is the fluctuation amplitude for the electrons and holes, respectively. This potential is characterized by zero-spatial average $\overline{V_{e,h}(\rho_{e,(h)})} = 0$ and a constant variance $\sigma_V^2 = \overline{V_{e,h}(\rho_{e,(h)})^2}$ (see Appendix A for mathematical details about the disorder potential). Apart from the random confinement disorder potential for electrons and holes, $V_{e,(h)}(\rho_{e,(h)})$, the electron-hole direct Coulomb interaction is treated here using the Rytova-Keldysh potential $V_{Ky}(\rho_e - \rho_h)$ according to the widely accepted approach [69–75], in order to take properly

into account the dielectric screening of the surrounding environment [10,11,69,71,75]. According to the effective mass theory and in the center-of-mass frame, the Hamiltonian can be written in the form

$$H = -\frac{\hbar^2 \nabla_{\rho}^2}{2\mu} + V_{Ky}(\rho) - \frac{\hbar^2 \nabla_{\mathbf{R}}^2}{2M_X} + V_e \left(\mathbf{R} - \frac{m_e}{M_X} \rho \right) + V_h \left(\mathbf{R} + \frac{m_h}{M_X} \rho \right). \quad (2)$$

Here, $\mathbf{R} = \frac{m_e \rho_e + m_h \rho_h}{m_e + m_h}$ and $\rho = \rho_e - \rho_h$ are the position vector of the exciton center of mass and relative distance of the electron from the hole, respectively, $M_X = m_e + m_h$ is the exciton mass, $\mu = \frac{m_e m_h}{m_e + m_h}$ is the reduced effective mass, and $\nabla_{\rho}, \nabla_{\mathbf{R}}$ are the gradient operators acting on the relative and center of mass coordinates, respectively.

We shall assume as working assumptions that (i) the random potential spatial correlation length is much larger than the free exciton Bohr radius a_b ($L > a_b$), so that the exciton internal motion is not perturbed by localization [76–78]. (ii) The perturbation introduced by disorder is not sufficient to produce a significant coupling between the $\tilde{1s}$ exciton state and higher excited states of the electron-hole motion [76–78]. Hence only the lowest bound state $\tilde{1s}$ at the fundamental sublevel transition will be considered. Here, $\tilde{n}s$ ($n \in \mathbb{N}^*$) represents the quasihydrogenoid series obtained for the free exciton using the Rytova-Keldysh potential (see Refs. [69,75]). Therefore the expectation expression of the effective random disorder potential $V_{e,(h)}(\rho_e, \rho_h)$ under this assumption is given by the expression

$$\begin{aligned} \hat{V}_{\tilde{1s}} &= \langle \chi_{\tilde{1s}} | V_e \left(\mathbf{R} - \frac{m_e}{M_X} \rho \right) + V_h \left(\mathbf{R} + \frac{m_h}{M_X} \rho \right) | \chi_{\tilde{1s}} \rangle \\ &= \frac{2\pi}{\sqrt{2N}} \sum_{i=1}^N \text{Re} \{ e^{i(\mathbf{K}_i \cdot \mathbf{R} + \phi_i)} \} \times \mathcal{I}(\tilde{1s}, \tilde{1s}, \mathbf{K}_i) \end{aligned} \quad (3)$$

with

$$\begin{aligned} \mathcal{I}(\tilde{1s}, \tilde{1s}, \mathbf{K}_i) &= \sum_{n,l} C(n,l) \sum_{n',l'} C(n',l') i^{l'-l} \\ &\times \int \varphi_n(\rho) \varphi_{n'}(\rho) \left[V_{0,e} J_{l'-l} \left(\frac{m_e}{M_X} K \rho \right) \right. \\ &\left. + V_{0,h} J_{l'-l} \left(\frac{m_h}{M_X} K \rho \right) \right] \rho d\rho. \end{aligned}$$

Here, $\chi_{\tilde{1s}}(\rho, \theta) = \sum_{n,l} C(n,l) \varphi_{n,l}(\rho, \theta)$ is defined in coordinate representation by the expansion in terms of 2D-hydrogenic states $\varphi_{n,l}(\rho, \theta)$ (see Refs. [69,75] for more details of the calculation of the wave function $\chi_{\tilde{1s}}(\rho, \theta)$) and $J_{l'-l}$ is the Bessel function of the first kind. By using the above assumption and for typical values of $V_{0e} = V_{0h} = V_0$, the effective random disorder potential, can be written as

$$\hat{V}_{\tilde{1s}}(\mathbf{R}) = \frac{V_0}{\sqrt{2N}} \sum_{i=1}^N \text{Re} \{ (e^{i(\mathbf{K}_i \cdot \mathbf{R} + \phi_i)}) \hat{f}(\tilde{1s}, \tilde{1s}, K) \} \quad (4)$$

with

$$\begin{aligned} \hat{f}(\tilde{1s}, \tilde{1s}, K) &\sim \left[1 + \left(\frac{2\pi m_h a_b^*}{4M_X L} \right)^2 \right]^{-\frac{3}{2}} \\ &+ \left[1 + \left(\frac{2\pi m_e a_b^*}{4M_X L} \right)^2 \right]^{-\frac{3}{2}}. \end{aligned}$$

Here, $K = |\mathbf{K}_i| = \frac{2\pi}{L}$, a_b^* is the effective Bohr radius in which we have taken into account the contribution of all the 2D hydrogenic states.

From Eq. (4), we can confirm under our assumption that the disorder affects only the center of mass motion (only the center of mass \mathbf{R} intervenes in $\hat{V}_{\tilde{1s}}$, and that this one is independent of $\rho = \rho_e - \rho_h$). We can notice also that in the region where $L \sim a_b^*$, we will just have an attenuation of the fluctuation amplitude, which results simply in decreasing V_0 . Although, in the limit of the small value of $L < a_b^*$, we will have a weak localization or even we will be in a regime with not any bound states in a disorder potential. Here, we will limit ourselves only to the case where L is much larger than a_b^* , ($L \gg a_b^*$), hence, in this limit, the potential $\hat{V}_{\tilde{1s}}$ can be written as follows:

$$\begin{aligned} \hat{V}_{\tilde{1s}}(\mathbf{R}) &= V(\mathbf{R}) \\ &= \sqrt{\frac{2}{N}} V_0 \sum_{i=1}^N \cos[\mathbf{K}(\theta_i) \cdot \mathbf{R} + \phi_i]. \end{aligned} \quad (5)$$

We can then separate the exciton center of mass and relative motion. The Hamiltonian of relative motion H_{rel} was largely studied in previous works [69,75]. Its eigenfunctions are denoted as $\chi_{\tilde{1s}}(\rho, \theta)$. The Hamiltonian that describes the localization of the center of mass motion by a disorder potential can be written in the envelope function approximation as follows:

$$H_{\text{cm}} = -\frac{\hbar^2 \nabla_{\mathbf{R}}^2}{2M_X} + V(\mathbf{R}). \quad (6)$$

Using the method of numerical diagonalization, we calculate the eigenvalues, $\hat{E}_{(j)}$, and the eigenfunctions, $\zeta_{(j)}(\mathbf{R})$, of this Hamiltonian. In order to solve the eigenvalue equation, we use a wave function expansion technique, where $\zeta_{(j)}(\mathbf{R})$ can be expanded using an auxiliary basis along with $\zeta_{(j)}(\mathbf{R}) = \sum_{n_x, n_y} D(n_x, n_y) \xi_{n_x, n_y}(X, Y)$. Here, $\xi_{n_x, n_y}(X, Y)$ are the wave functions of a 2D harmonic oscillator, which are constructed using the Hermite polynomials \mathbf{H}_{n_x, n_y} and are given by

$$\begin{aligned} \xi_{n_x, n_y}(X, Y) &= \frac{1}{\sqrt{n_x! n_y!}} \frac{1}{\sqrt{2^{n_x, n_y}}} \sqrt{\frac{1}{\pi R_{\text{cm}}^2}} \mathbf{H}_{n_x} \left(\frac{X}{R_{\text{cm}}} \right), \\ \mathbf{H}_{n_y} \left(\frac{Y}{R_{\text{cm}}} \right) &e^{-\frac{X^2}{2R_{\text{cm}}^2}} e^{-\frac{Y^2}{2R_{\text{cm}}^2}}. \end{aligned}$$

In this notation, the integers n_x, n_y are quantum numbers, $R_{\text{cm}} = \sqrt{\frac{\hbar}{M_X \omega_{\text{cm}}}}$ is the center of mass localization radius in the harmonic potential description, and ω_{cm} is the frequency of a 2D harmonic oscillator. The coefficients $D(n_x, n_y)$ are obtained by solving the matrix problem with eigenfunctions $\zeta_{(j)}(\mathbf{R})$ and eigenvalues $\hat{E}_{(j)}$. Here, the number (j) labels the

eigenstates and refers to the dominant contribution of the coefficients $D(n_x, n_y)$. In the numerical calculations, the number of basis functions $\xi_{n_x, n_y}(X, Y)$ should be finite. Usually, the basis functions are chosen provided that they are the lowest energy states of the Hamiltonian. This approach leads to a good convergence of the eigenvalues as a function of the number of basis states. Therefore the solutions of the resulting Schrödinger equation of the system satisfy the eigenequation $(H_{\text{cm}} + H_{\text{rel}})\Upsilon_{(\tilde{s}, j)}(\mathbf{R}, \boldsymbol{\rho}) = E_{(\tilde{s}, j)}\Upsilon_{(\tilde{s}, j)}(\mathbf{R}, \boldsymbol{\rho})$, and are given by $\Upsilon_{(\tilde{s}, j)}(\mathbf{R}, \boldsymbol{\rho}) = \zeta_{(j)}(\mathbf{R})\chi_{\tilde{s}}(\boldsymbol{\rho}, \theta)$ and $E_{(\tilde{s}, j)} = E_g + \hat{E}_{(j)} + E_{\tilde{s}}$.

We note that the choice of the basis functions, which are Hermite polynomials multiplied by Gaussian functions, is based on the fact that we treat only the case where the excitonic states are located in the potential well, i.e., the energy levels are small compared to the fluctuation potential amplitude, which can be verified only if $V_0 > \hbar\omega_{\text{cm}}$. In the opposite case ($V_0 < \hbar\omega_{\text{cm}}$), the center of mass wave function of the localized exciton cannot be described in the used basis (the choice of the basis function will be discussed in detail in the next paragraph and in Appendix B).

In the presence of a random disorder potential, the translational symmetry of the crystal is broken so that the momentum of the center of mass motion is no longer a good quantum number as was assumed in the previous model related to the free exciton [58,69,75]. The exciton in monolayer TMDs behaves as a massive particle subject to a disordered potential, leading to spatially localized eigenstates of the center of mass motion [35,58,77,78] and, therefore, as we shall see, to long exciton emission lifetimes with respect to the exciton intrinsic recombination time [6,61].

B. Relevant parameter range for the model

We discuss now the impact of the characteristic parameters of the disorder correlation length and potential fluctuations amplitude on the outcome of the simulations. This provides us with further insights into the structure of the single exciton states and their optical properties. The center of mass exciton motion defined by Hamiltonian (6) and the random disorder potential (5) depends on the two reduced independent parameters, $\frac{L}{R_{\text{cm}}}$ and $\frac{V_0}{\hbar\omega_{\text{cm}}}$. In fact, since R_{cm} constitutes the natural length unit for the Schrodinger problem and $\hbar\omega_{\text{cm}}$ is the corresponding unit of energy, we can drive the scaling properties of the matrix element of the center of mass motion by using these two units. Therefore the matrix elements of $\hat{H}_{\text{cm}} = \frac{H_{\text{cm}}}{\hbar\omega_{\text{cm}}}$ are rewritten as follows:

$$\begin{aligned} \langle \xi_{n_x, n_y} | \hat{H}_{\text{cm}} | \xi_{n'_x, n'_y} \rangle &= \langle \tilde{E}_c \rangle_{n_x, n_y, n'_x, n'_y} + \langle \tilde{E}_p \rangle_{n_x, n_y, n'_x, n'_y} \\ &= \langle \tilde{E}_c \rangle_{n_x, n_y, n'_x, n'_y} + \frac{V_0}{\hbar\omega_{\text{cm}}} \\ &\quad \times \sum_{i=1}^N \mathcal{F}(n_x, n_y, n'_x, n'_y, \alpha_i, \beta_i). \end{aligned} \quad (7)$$

The kinetic term in the equation is $\langle \tilde{E}_c \rangle_{n_x, n_y, n'_x, n'_y}$. The discussion will focus on the second term in the equation by evaluating the potential energy $\langle \tilde{E}_p \rangle_{n_x, n_y, n'_x, n'_y}$. These two contributions are described in more details in Appendix B. Here,

$\alpha_i = 2\pi \frac{R_{\text{cm}}}{L} \cos(\theta_i)$, $\beta_i = 2\pi \frac{R_{\text{cm}}}{L} \sin(\theta_i)$. The tilde denotes here scaled quantities with R_{cm} being the length unit and $\hbar\omega_{\text{cm}}$ the energy unit. In this paper, we revisit our theoretical model given in Ref. [69] and check systematically the impact of the different characteristic parameters V_0 and L . We will discuss in the next paragraph the choice of correlated auxiliary basis parameters $\hbar\omega_{\text{cm}}$ and R_{cm} .

1. Choice of the auxiliary basis energy parameter $\hbar\omega_{\text{cm}}$ relatively to the disorder parameter fluctuation amplitude V_0

In order to justify the choice of the basis, we study the effect of $\hbar\omega_{\text{cm}}$ compared to V_0 for a fixed value of the correlation length L (within the condition $L \gg a_b^*$). In fact, two domains are of importance: $\hbar\omega_{\text{cm}} < V_0$ and $\hbar\omega_{\text{cm}} > V_0$.

As shown in paragraph 1 of Appendix B, the choice of the harmonic oscillator basis is only valid if the energy levels found are lower than the potential fluctuations so the solutions found are relatively accurate. Hence, in order to respect this condition, it is necessary to restrict our calculations to the case $\hbar\omega_{\text{cm}} < V_0$. In this case, the center of mass eigenenergies satisfy $\hat{E}_{(j)} < 0$, which means that excitons are localized in deep potential traps associated with certain types of impurities, such as local strain or edge states at the sample boundaries. In the opposite case, $\hbar\omega_{\text{cm}} > V_0$, we can obtain positive values of the center of mass energies. However, the states obtained then are unphysical since they cannot be described, in principle, in the frame of our model using only one type of basis functions (see Appendix B). This case would lead, in principle, to unbound exciton states in a random potential, whose description is out of the scope of the present paper.

2. Choice of the auxiliary basis localization parameter R_{cm} relatively to the disorder parameter correlation length L

For a fixed value of V_0 , we study the effect of the harmonic localization length R_{cm} compared to the correlation length L . In fact, since R_{cm} is determined by $\hbar\omega_{\text{cm}}$, then the choice of the range of R_{cm} value has to be compatible with the condition $\hbar\omega_{\text{cm}} < V_0$, which implies that $R_{\text{cm}} > \frac{\hbar}{\sqrt{M_X V_0}}$. From Eq. (7) and with respect to these considerations, we study two limiting cases.

(i) If $R_{\text{cm}} \ll L$, the potential energy $\langle \tilde{E}_p \rangle_{n_x, n_y, n'_x, n'_y}$ will increase with the increase of the ratio $\frac{L}{R_{\text{cm}}}$, i.e., with the increase of L . This can lead to strong disorder and large correlation length L , hence, to stronger confinement excitonic energies. Therefore the shift between the neutral exciton and the first state of localized exciton ($\Delta E = E_{X_0} - E_{LX_1}$) increases with the increase of the ratio $\frac{L}{R_{\text{cm}}}$. This effect introduces confinement in all directions like in the well-known cases of excitons in a quantum dot potential or in narrow semiconductor quantum wells with fluctuating thickness grown with molecular beam epitaxy [35,76–78].

(ii) If $R_{\text{cm}} \gg L$, the potential energy $\langle \tilde{E}_p \rangle_{n_x, n_y, n'_x, n'_y}$ will decrease with the increase of the ratio $\frac{L}{R_{\text{cm}}}$, i.e., with increasing L . Therefore the shift ΔE decreases with the increase of the ratio $\frac{L}{R_{\text{cm}}}$. This can lead to a weak disorder with short correlation length L .

In summary, the disorder effect on the excitonic properties can be controlled by the choice of the appropriate parameter

range. In fact, (i) to get sufficient accuracy in the numerical calculation of the eigensolutions, (ii) to take into account the details of the fluctuation potential with sufficient spatial resolution, and (iii) in order to not perturbate the exciton internal motion by the disorder potential, the harmonic localization length R_{cm} has to satisfy the double inequality

$$a_b^* \ll R_{\text{cm}} < L.$$

On the other hand, in order to find a bound state of energy, which is lower than the free exciton, and to ensure the agreement with experimental findings, we must also satisfy the inequality

$$\hbar\omega_{\text{cm}} < V_0.$$

Hence we end up with the framing

$$\sup\left(a_b^*, \frac{\hbar}{M_X V_0}\right) \langle R_{\text{cm}} \rangle L. \quad (8)$$

For a fixed value of L , one will be able to test with a given auxiliary basis different values of V_0 satisfying this inequality:

$$\sup\left(\frac{\hbar^2}{M_X L^2}, \hbar\omega_{\text{cm}}\right) \langle V_0 \rangle. \quad (9)$$

We note that at this stage we do not make any further assumptions for the disordered potential $V(X, Y)$. We point out, however, that the optical properties of the localized exciton are characterized by typical values of the correlation length L , and a potential amplitude fluctuation V_0 that will be discussed in the next section.

C. Calculation of radiative lifetime

Once the exciton wave functions have been obtained by diagonalizing the Hamiltonian of the localized exciton, using the dipole matrix elements relevant to interband optical transitions, we can calculate the radiative lifetime of localized excitons in monolayer TMDs under the approximations stated above. Since we work at low temperature and under low-density excitation, (i) we do not take into account the thermalization processes. In this work, we do not include scattering by optical phonons, assuming the excitonic temperature to be much lower than the optical phonon energy (30 meV for WSe₂) [61,64,79]. Moreover, we assume that the phonon spontaneous emission by localized excitons is negligible. (ii) Besides, since we have assumed low excitation conditions, i.e., low exciton density, exciton-exciton scattering and exciton annihilation processes are inefficient [61,64,79]. Therefore they can be ignored when calculating the exciton radiative lifetimes. (iii) On the other hand, as we said previously, TMDs can exhibit bright, dark, and Z-mode excitons [15,52,54,61]. Dark exciton states do not couple directly to radiation and thus they will not be considered here [61,64]. The localized Z-mode excitons [15], which couple to in-plane propagating optical modes with polarization perpendicular to the TMD plane, could be also calculated in a similar manner. However, we will disregard them here, since they emit at lower energies and their oscillator strength is quite weak with respect to bright excitons [64].

We start by giving a theoretical description of the spontaneous emission due to the interaction of the localized

excitons with the continuum of vacuum photon modes. In the Coulomb gauge, the light-matter interaction is described by the Hamiltonian $\hat{H}_{\text{int}} = \frac{e}{m_0 c} \mathbf{p} \cdot \mathbf{A}(\mathbf{r}, t)$, where e is the elementary charge, \mathbf{p} is the electron momentum operator, c is the light velocity, and $\mathbf{A}(\mathbf{r}, t)$ is the vector potential operator in the second quantization:

$$\mathbf{A}(\mathbf{r}, t) = \sum_{\mathbf{q}, \lambda} \sqrt{\frac{2c\pi\hbar}{qVn_0}} \left\{ \epsilon_{\mathbf{q}}^{(\lambda)} a_{\mathbf{q}}^{(\lambda)} e^{i(\mathbf{q}\cdot\mathbf{r} - \omega_{\mathbf{q}}t)} + \epsilon_{\mathbf{q}}^{(\lambda)} a_{\mathbf{q}}^{\dagger(\lambda)} e^{-i(\mathbf{q}\cdot\mathbf{r} - \omega_{\mathbf{q}}t)} \right\}. \quad (10)$$

Here, the sum is extended to all plane-wave eigenmodes (\mathbf{q}, λ) within a normalization volume $V = L_z S$ (S is the TMD surface), and $\epsilon_{\mathbf{q}}^{(\lambda)}$ is a unit vector characterizing the optical mode polarization λ . The operator $a_{\mathbf{q}}^{\dagger(\lambda)}$ ($a_{\mathbf{q}}^{(\lambda)}$) creates (annihilates) a photon with wave vector \mathbf{q} and polarization λ . For a given eigenmode, the optical angular frequency is defined by $\omega_{\mathbf{q}} = \frac{c}{n_0} |\mathbf{q}|$, where $n_0 = \sqrt{\frac{\epsilon_1 + \epsilon_2}{2}}$ is the effective optical refraction index of the crystal environment.

The light-matter coupling can be evaluated in the basis $\{|\dots, n_{\mathbf{q}, \lambda} \dots\rangle \otimes |\Phi_{(j)}^v\rangle\}$. Here, $\{|\dots, n_{\mathbf{q}, \lambda} \dots\rangle\}$ are the electromagnetic field states in Fock representation. The solution of the Schrodinger equation for a localized exciton in a solid is

$$\Phi_{(j)}^v(\mathbf{R}, \boldsymbol{\rho}) = \Upsilon_{(j)}(\mathbf{R}, \boldsymbol{\rho}) \mathcal{U}^{\gamma_x}(\mathbf{r}_e, \mathbf{r}_h), \quad (11)$$

where $\Upsilon_{(j)}(\mathbf{R}, \boldsymbol{\rho})$ is the envelope function described in Sec. II, and $\mathbf{r}_e = (\boldsymbol{\rho}_e, z_e)$ and $\mathbf{r}_h = (\boldsymbol{\rho}_h, z_h)$ are the electron and hole spatial coordinates, respectively. The function $\mathcal{U}^{\gamma_x}(\mathbf{r}_e, \mathbf{r}_h) = \sum_{\alpha_c, \alpha_h} C_{c, \alpha_c; h, \alpha_h}^{\gamma_c, \gamma_h} U_{c, \alpha_c}^{\gamma_c}(\mathbf{r}_e) U_{h, \alpha_h}^{\gamma_h}(\mathbf{r}_h)$ represents the combination of electron and hole Bloch amplitude products transforming according to the representation γ_x of the D_{3h} symmetry group in coordinate representation [52]. Here, $|U_{c, \alpha_c}^{\gamma_c}\rangle$ ($|U_{h, \alpha_h}^{\gamma_h}\rangle$) is the conduction (hole) Bloch amplitude transforming along the representation γ_c (γ_h) of D_{3h} symmetry group, and $\alpha_{c(h)} = (\tau_{c(h)}, s_{c(h)})$ characterize the single-particle valley ($\tau_c = \pm 1$) and effective spin ($s_c = \pm \frac{1}{2}$) indices. The hole state is related to the valence electron state by $|U_{h, \alpha_h}^{\gamma_h}\rangle = \hat{K} |U_{v, \alpha_v}^{\gamma_v}\rangle$, \hat{K} being the time-reversal operator [80], and the coefficients $C_{c, \alpha_c; h, \alpha_h}^{\gamma_c, \gamma_h}$ are deduced from Refs. [15,81]. According to the time-dependent perturbation theory, the radiative lifetime is calculated using Fermi's golden rule $\tau_{\text{rad}}^{-1} = \frac{2\pi}{\hbar} |\langle i | H_{\text{int}} | f \rangle|^2 \delta(E_i - E_f)$. The initial state consists of an excitonic state without a photon $|i\rangle = |\Phi_{(j)}^v\rangle \otimes |0_{\mathbf{q}, \lambda}\rangle$, while the final state consists of the crystal ground state $|\emptyset\rangle$ with one photon $|f\rangle = |\emptyset\rangle \otimes |1_{\mathbf{q}, \lambda}\rangle$. Therefore the probability of spontaneous emission of a photon in the mode (\mathbf{q}, λ) per time unit is then given by

$$P_{(j), \mathbf{q}, \lambda} = \frac{(2\pi)^2 e^2}{n_0 m_0^2 c V q} |M_{(j), \mathbf{q}, \lambda}|^2 \delta(\hbar\omega_j^X - \hbar\omega_{\mathbf{q}}). \quad (12)$$

Here, δ function ensures the energy conservation between the localized exciton ($E_{\tilde{s}, (j)} = \hbar\omega_j^X$) and the photon ($\hbar\omega_{\mathbf{q}}$). We note that for each direction of propagation \mathbf{q} of emitted photon, there are two independent linear polarizations λ . The factor $M_{(j), \mathbf{q}, \lambda} = \langle \Phi_{(j)}^v | \hat{H}_{\mathbf{q}}^{(\lambda)} | \emptyset \rangle$ is the optical matrix element characterizing the transition from the 2D crystal ground state to the exciton state $|\Phi_{(j)}^v\rangle$. For direct excitons, it can be

presented under the form

$$M_{(j),\mathbf{q},\lambda} = \overline{\zeta_j}(\mathbf{K}_X = 0) \chi_{\Gamma_s}(\rho = 0) \times \sum_{\alpha_c, \alpha_h} C_{c,\alpha_c;h,\alpha_h}^{\gamma_c, \gamma_h} \langle U_{c,\alpha_c}^{\gamma_c} | \epsilon_{\mathbf{q}}^{(\lambda)} \cdot \hat{\mathbf{p}} | U_{v,\alpha_h}^{\gamma_h} \rangle, \quad (13)$$

where $\overline{\zeta_j}(\mathbf{K}_X = 0) = \int \int \zeta_j(\mathbf{R}) d^2R$ represents the Fourier transform of the center of mass wave function taken at $\mathbf{K}_X = 0$. We have used the fact that the Bloch functions are orthogonal, the envelope functions are slowly varying on the scale of the lattice parameter, and the wave vector \mathbf{q} is negligible compared to the size of the Brillouin zone. By summing $P_{\mathbf{q},\lambda}$ over all the photon modes (\mathbf{q}, λ) , $P_j = \sum_{\mathbf{q}} P_{\mathbf{q},\lambda}$, we obtain

$$P_{(j)} = \frac{e^2}{2\pi \hbar c^3 m_0^2} n_0 \omega_j^X \left| \sum_{n_x, n_y} D(n_x, n_y) \int \xi_{n_x, n_y}(\mathbf{R}) d^2\mathbf{R} \right|^2 \times |\chi_{\Gamma_s}(\rho = 0)|^2 \mathcal{I}. \quad (14)$$

In the above equation, the factor $\mathcal{I} = \sum_{\lambda=1,2} \int_0^\pi \int_0^{2\pi} d\theta d\phi \langle U_{c,\alpha_c}^{\gamma_c} | \epsilon_{\mathbf{q}}^{(\lambda)}(\theta, \phi) \cdot \hat{\mathbf{p}} | U_{v,\alpha_h}^{\gamma_h} \rangle|^2$ represents the angular integral over all the photon modes (including their polarization) that can be spontaneously emitted. The matrix element $\langle U_{c,\alpha_c}^{\gamma_c} | \epsilon_{\mathbf{q}}^{(\lambda)} \cdot \hat{\mathbf{p}} | U_{v,\alpha_h}^{\gamma_h} \rangle = \epsilon_{\mathbf{q}}^{(\lambda)} \cdot \langle U_{c,\alpha_c}^{\gamma_c} | \hat{\mathbf{p}} | U_{v,\alpha_h}^{\gamma_h} \rangle$ appearing in the integral \mathcal{I} depends on the nature of the Bloch functions and the photon polarization $\epsilon_{\mathbf{q}}^{(\lambda)}$, and the coupling term $\langle U_{c,\alpha_c}^{\gamma_c} | \hat{\mathbf{p}} | U_{v,\alpha_h}^{\gamma_h} \rangle$ can be found in Koster tables within a constant proportionality coefficient [81], yielding the exciton chiral selection rules. Taking into account the emission of bright excitons only [15], we obtain $|\psi_{\pm}^{\Gamma_6}\rangle = |U_{c,\pm 1, \pm 1/2}^{\Gamma_9}\rangle |U_{h,\mp 1, \mp 1/2}^{\Gamma_7}\rangle$ which belongs to Γ_6 representation of D_{3h} . The only nonzero elements of the valence-conduction coupling terms are $\langle U_{c,\pm 1, \pm 1/2}^{\Gamma_9} | \hat{p}_{\pm} | U_{v,\mp 1, \mp 1/2}^{\Gamma_7} \rangle = \pm \Pi_{\perp}$ for circularly polarized light σ_{\pm} propagating along the normal to the sample ($p_{\pm} = \frac{p_x \pm ip_y}{\sqrt{2}}$), so that only optical modes with in-plane polarization components couple to these excitons. The quantity Π_{\perp} can be approximately evaluated by using the $\mathbf{k} \cdot \mathbf{p}$ two-band model [54,67]. In that case, it is given by $\Pi_{\perp} = \sqrt{\frac{m_0 E_p}{2}}$, where $E_p = \frac{m_0 E_g}{m_e^*}$ is the Kane energy for TMDs obtained in the two-band model. Here, the carrier effective mass will be in turn estimated from DFT calculations. The integral \mathcal{I} is given by $\mathcal{I} = \frac{16\pi}{3} |\Pi_{\perp}|^2$. Finally, we obtain for the spontaneous emission rate of localized exciton state j :

$$P_{(j)} = \frac{4e^2}{3\hbar m_0 c^3} n_0 \omega_j^X E_p |\chi_{\Gamma_s}(\rho = 0)|^2 \times \left| \sum_{n_x, n_y} D(n_x, n_y) \int \xi_{n_x, n_y}(\mathbf{R}) d^2\mathbf{R} \right|^2. \quad (15)$$

Using the above relation, we can now calculate the radiative lifetime of localized excitons $\tau_j = \frac{1}{P_{(j)}}$.

Having described in this section the theoretical model, we turn now to individual excitonic states in specific disorder realizations. According to the experimental considerations, we can envisage several scenarios of disorder. In our study, by the variation of appropriate parameters L and V_0 , we realize

different cases of disorder: weak, mean, or strong disorder. We start the discussion with the effect of the correlation length L . Later, we will study the effect of the potential amplitude fluctuations V_0 .

III. IMPACT OF THE CORRELATION LENGTH ON THE EXCITON STATES IN SINGLE DISORDER REALIZATIONS

To investigate the effect of L on the excitonic properties, we carry out several simulations for different values of L and given disorder realization. In the following, three realizations I, II, and III of disorder potential are discussed and compared, having fixed V_0 , N , $\hbar\omega_{\text{cm}}$, and R_{cm} parameters but varying the value of L . The simulated potential landscapes $V_{I,II,III}(\mathbf{R})$ for the three simulations are shown in the panel of Figs. 1(a)–1(c). One can observe the localized states energies in Figs. 1(d)–1(f), probability density function in Figs. 2(a)–2(c), exciton photoluminescence peaks in Figs. 3(a)–3(c), as well as their corresponding radiative lifetime Figs. 3(d)–3(f).

A. The disorder potential

For WSe₂ monolayer deposited on the top of the SiO₂ substrate and exposed to the air taking $m_e = 0.48m_0$, $m_h = 0.44m_0$ [82] and for $N = 1000$, $V_0 = 110$ meV, $R_{\text{cm}} = 30$ Å, and $L = 2.3R_{\text{cm}} = 70$ Å [simulation I illustrated in Fig. 1(a)], $L = 5R_{\text{cm}} = 150$ Å [simulation II plotted in Fig. 1(b)], $L = 20R_{\text{cm}} = 600$ Å [simulation III shown in Fig. 1(c)], the

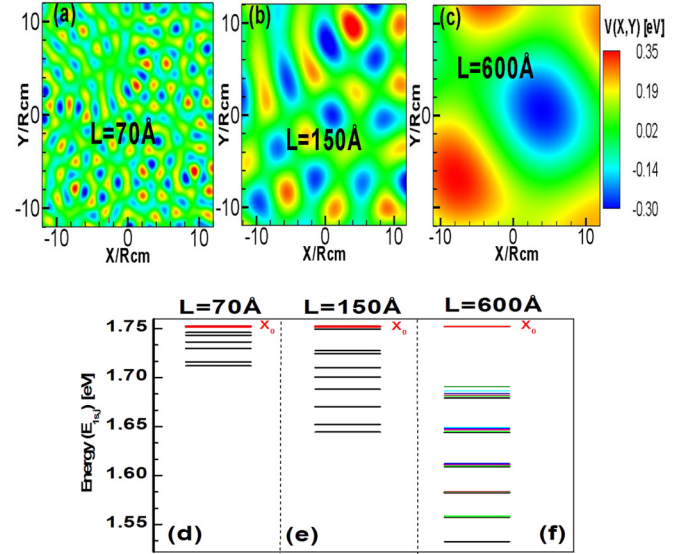


FIG. 1. Spatial map of disorder potential. (a)–(c) Contour plot of the inhomogeneous landscape, showing lakes and hills; and (d)–(f) the corresponding eigenenergies of the localized excitons obtained by the numerical diagonalization of the matrix resulting from the projection of the Hamiltonian H [Eq. (6)] and localized in the disorder potential given by Eq. (5). We restrict ourselves only to the states $E_{\Gamma_s, j}$ smaller than the free exciton energy (1752 eV). The values of $N = 1000$, $V_0 = 110$ meV, $R_{\text{cm}} = 30$ Å are fixed, and we vary the correlation length L ; [(a) and (d)] $L = 70$ Å (simulation I); [(b) and (e)] $L = 150$ Å (simulation II), and [(c) and (f)] $L = 600$ Å (simulation III). The monolayer WSe₂ is deposited on the SiO₂/Si substrate and exposed to the air.

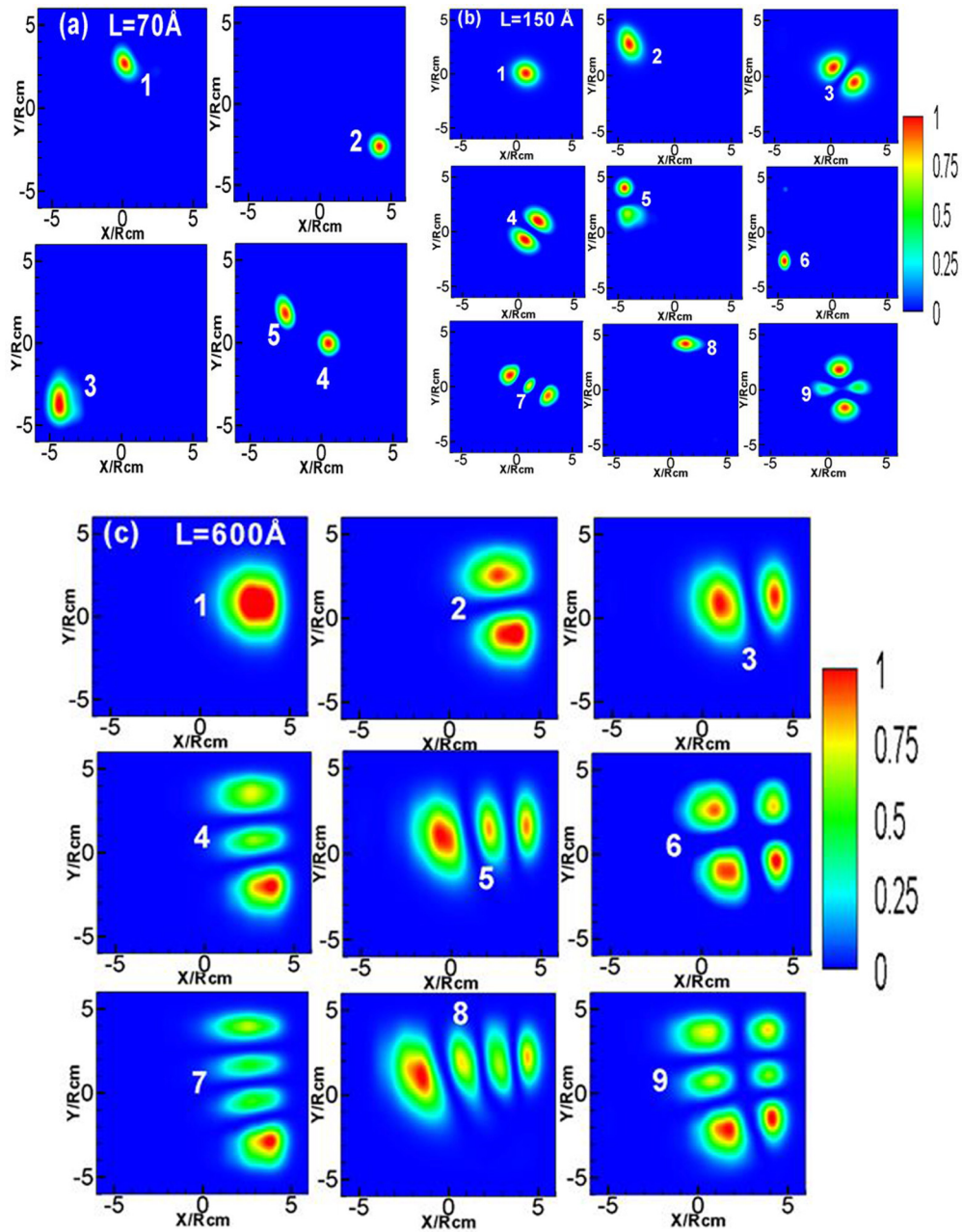


FIG. 2. Probability density distribution of selected excitonic states for fixed values of $N = 1000$, $V_0 = 110$ meV, $R_{cm} = 30$ Å and various values of L ; (a) $L = 70$ Å (simulation I); (b) $L = 150$ Å (simulation II), and (c) $L = 600$ Å (simulation III). The color scale is the normalized probability, which shows the spatial distribution of the main low-lying states contributing to the LX_j . The monolayer WSe_2 is deposited on the SiO_2/Si substrate and exposed to the air.

disorder potential is characterized by several inhomogeneous lakes (wells) and hills having different trenches of quasicircular or more or less elongated and irregular shape [83]. These lakes constitute the potential traps that localize the exciton center of mass motion.

They are randomly distributed over the whole space extent of the simulation. Indeed, these images prove the random nature of the disorder potential. Interestingly, the distributions, the heights, the depths, the numbers of peaks, wells, and the form of potential are different from one simulation to another, i.e., for different correlation lengths. This can lead

to a variation in the confinement and therefore a variation of the energies, the waves function, the oscillator strength and the radiative lifetime, which are the characteristic features of localized excitons. Moreover, we notice from these figures that for a given region of space (here 12.5×12.5 in the unit of R_{cm}), when L increases, the numbers of lakes and hills decreases. For example, for $L = 70$ Å [Fig. 1(a)], we have several peaks and wells, while the disorder potential is characterized by a single large well when L becomes much greater than the center of mass radius R_{cm} ($L \gg R_{cm}$) [Fig. 1(c)]. Also, we observe the extension of the wells width

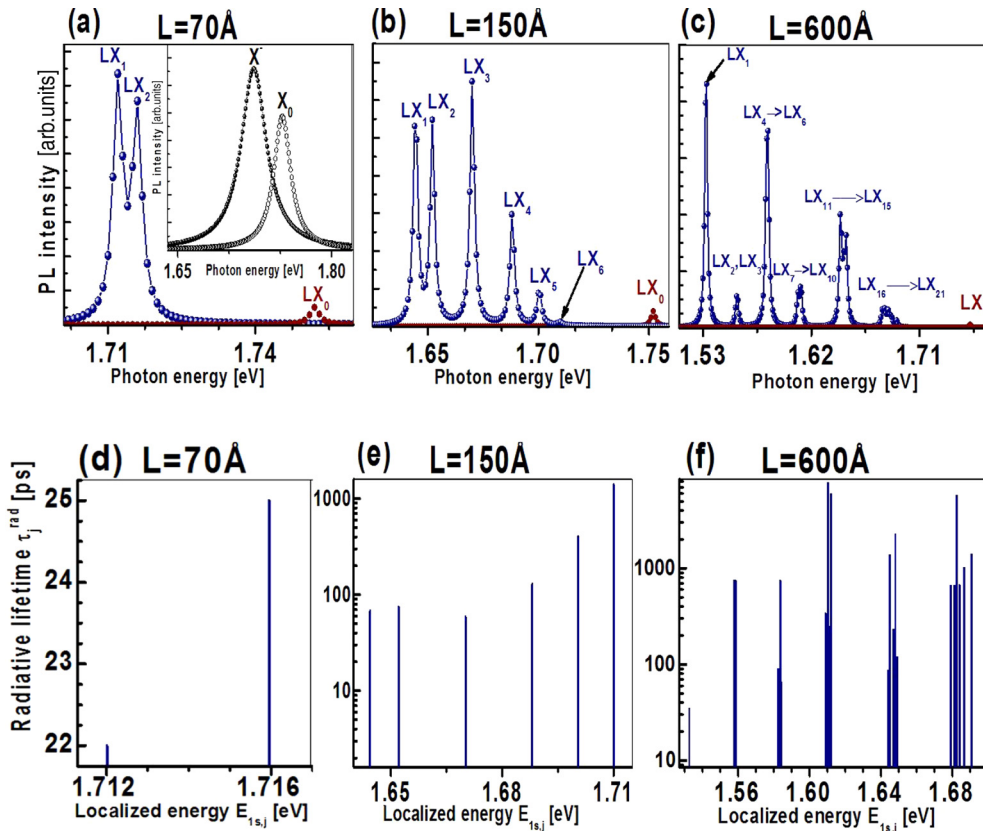


FIG. 3. (a)–(c) PL spectrum of defects from monolayer WSe₂ LX_j , (d)–(f) the corresponding radiative lifetime calculated using Eq. (15) for fixed values of $N = 1000$, $V_0 = 110 \text{ meV}$, $R_{cm} = 30 \text{ \AA}$, and various values of L ; [(a) and (d)] $L = 70 \text{ \AA}$ (simulation I); [(b) and (e)] $L = 150 \text{ \AA}$ (simulation II), and [(c) and (f)] $L = 600 \text{ \AA}$ (simulation III); in the inset, the PL spectrum of the neutral free exciton and trion from a pristine region of a monolayer WSe₂ calculated in the previous study [75]. The observed low-energy PL peaks are assigned to emissions from localized excitons trapped in the random potential induced by disorder. Note that the localized states are located below the neutral free exciton peak and the values of radiative lifetime range from tens of picosecond to nanoseconds. The monolayer WSe₂ is deposited on the SiO₂/Si substrate and exposed to the air.

with the increase of L . This can lead to a stronger confinement for a given fluctuation amplitude V_0 and therefore to a more localized excitonic states.

B. Localized excitonic energies

According to the previous simulations, we plot in the panels of Figs. 1(d)–1(f), the first energy levels of the excitonic states $E_{1s,j}$ located in the disorder potential given by Eq. (5). These solutions are obtained by solving the Hamiltonian H [Eq. (6)]. From the realizations I and II [Figs. 1(d) and 1(e)], we found that the localized exciton series in ML WSe₂ deviates significantly from a two-dimensional (2D) harmonic oscillator in two significant ways. (i) First, the spacings between the energy levels of the localized excitons are no longer equidistant. For example, in the simulation II when $L = 150 \text{ \AA}$, the spacing between the second and the first levels $\delta E_{(2),(1)}$ is equal to 7.65 meV , while the spacing between the third and the second level is equal to $\delta E_{(3),(2)} = 18 \text{ meV}$. We note that the difference between states is smaller than the fluctuation amplitude V_0 ($V_0 \gg \delta E_{(j+1),(j)}$). (ii) In addition, in a 2D harmonic oscillator with cylindrical symmetry, the states are $(n + 1)$ -fold degenerate (with $n = n_x + n_y$, and $n_x, n_y = 0, 1, \dots$); however, our calculations show clearly that a

splitting of these multiplets can arise due to cylindrical symmetry breaking of the local potential wells, leading to reduced degeneracy of excited orbital states. We checked that the splitting between the first energy levels of localized excitons is smaller than the $1s - 2s$ splitting of the free excitons, thus justifying our assumption that only $1s$ states are considered in our truncated basis set. The energy-level splitting is determined by a strong spatial localization of the exciton center of mass in the disorder potential while the deviation from the harmonic oscillator series is determined by the anharmonicity of the disorder potential. Although these two simulations present the same features, the confinement energies and the spacing of the energy levels are completely different. For realization III, we use the same $V_0 = 110 \text{ meV}$ and $R_{cm} = 30 \text{ \AA}$ as the other simulations but an L much greater than the previous simulation ($L = 600 \text{ \AA}$). From Fig. 1(f), we can notice that the lowest states of the exciton series is now roughly conform to a 2D harmonic oscillator with a quasi $-(n + 1)$ -fold degeneracy and an approximate equidistance between consecutive energy levels. For that we can use the same notation as a 2D harmonic oscillator. However, this simple description becomes inadequate for the highest excited states, since the local Gaussian disorder potential deviates strongly from the parabolic approximation in this energy range. As a matter

of fact, in simulations I and II, there are several localization sites, which lead to the superposition of several, more or less, harmonic states (hence the apparent anharmonicity of the state when we superimpose all these levels), whereas there is only a single well in simulation III for the surface considered, hence the approximate harmonic scale observed in this simulation for the lowest energy levels.

C. Probability densities of localized excitons

Following the study of the effect of L on the energy, we turn now to discuss its effect on the probability densities of the center-of-mass wave function for the three different simulations. According to the profile plotted in Figs. 1(a)–1(c), we display in Figs. 2(a)–2(c) the square modulus of some exciton center of mass wave functions selected among the lowest-energy eigenstates. In these panels, the excitonic states are labeled by an eigenstate number j , sorted in order of ascending eigenenergies \tilde{E}_j . We begin the discussion with realization I, see Fig. 2(a). We have therefore chosen to plot in each panel several states having similar features, according to the discussion below. We notice that for realization I, most of the states below the neutral exciton PL peak are attributed to the local ground states of the exciton center of mass because they are formed by a single lobe. These states have a dominant contribution from a local ground solution, as expected. Indeed, since the localization length is small, the confinement energy is large, so that the confinement of exciton excited states is not likely to occur at the local minimum of the narrow 2D quantum wells resulting from the disorder potential. The probability densities of the center of mass wave function in real space for the first few states of the realization II are illustrated in Fig. 2(b). The nodal structure of the wave functions is observed in this plot. The state 1 is the exciton ground state of the considered area and thus also a local ground state. States 2, 6, and 8 show a similar behavior, and should thus be attributed to local ground states because they are formed by a single lobe, i.e., have a dominant contribution from a local ground solution. States 3 and 4 (with 2 lobes) are the first excited states of the local well corresponding to the fundamental state 1, while states 7 (3 lobes) and 9 (4 lobes) are further excited states of the same well. This well is located in the middle of the sample. Similarly, state 5 (2 lobes) is an excited state of the local well corresponding to the fundamental state 2. All these states are localized in a local minimum of the disorder potential. In comparison with the realization I, we can say generally that while all the states of the simulation I are characterized only by ground states, most of the states in realization II are well described by ground and excited states. For the simulation III, the probability density of states is shown in Fig. 2(c). We notice that these densities share similar in-plane nodal structures with the excited states of a two-dimensional harmonic oscillator, which have the degeneracies 1, 2, 3, 4, ..., and therefore enable the eigenstates to be labeled with principal quantum number $(\tilde{n}_x, \tilde{n}_y)$, where this notation marks the dominant contribution to the eigenstate (j) of the (n_x, n_y) harmonic state. Unlike the previous cases, all these states are located in the same place, these results are predicted since our potential is characterized by a single well in the simulated region. State 1 (with only one lobe)

in Fig. 2(c) is attributed to the local ground state, which is nondegenerate: to this state, we can associate the wave function $\zeta_{\tilde{0},\tilde{0}}(\mathbf{R})$. States 2 and 3 with two lobes correspond to the second and third excited states. They are nearly twice degenerate and correspond to approximately the wave function $\zeta_{\tilde{1},\tilde{0}}(\mathbf{R})$ and $\zeta_{\tilde{0},\tilde{1}}(\mathbf{R})$, respectively. These states are already quite deformed due to the nonperfect cylindrical symmetry of the potential trench. Let us note that all these calculations concern only the orbital part of the center of mass exciton motion. The orbital bright exciton states should present an additional spin degeneracy. One can anticipate that the latter is removed by the long-range electron-hole exchange when the slightly elongated shape of the confinement potential breaks the cylindrical symmetry, as is well known in the case of self-assembled quantum dots.

D. Photoluminescence spectroscopy of the localized exciton:

We calculate now the PL spectrum at $T = 4$ K using the following expression:

$$P^{LX_j} \propto |\chi_{\tilde{1}s}(\rho = 0)|^2 \sum_{n_x, n_y} D(n_x, n_y) \int \xi_{n_x, n_y}(X, Y), dXdY |\mathcal{L}(\hbar\omega - E_{\tilde{1}s, j})|, \text{ where the Lorentzian } \mathcal{L}(\hbar\omega - E_{\tilde{1}s, j}) = \frac{\gamma}{\pi[(\hbar\omega - E_{\tilde{1}s, j})^2 + \gamma^2]}$$

express the energy conservation taking into account the state broadening. Here, the phenomenological parameter γ is the half width at half maximum of the lines, taken here as an arbitrary constant. The calculated spectra display several anharmonic peaks, which simulate in a realistic manner the low-energy peaks observed experimentally.

In Figs. 3(a)–3(c), we reproduce the multiple emission peaks observed in ML WSe₂ for different values of L (70, 150, and 600 Å). We note that the PL features LX_j are attributed to the localized exciton states from the region with defects. For comparison, the free exciton line X_0 (from a pristine monolayer) deduced from a former work [69,75] for a homogeneous sample is put in the inset of Fig. 3(a). In low-quality samples with high defect density or nonencapsulated samples, we see irregular comblike lines at low energy in the PL spectra: this kind of spectrum differs significantly from the spectral characteristics of pristine WSe₂ monolayer where only two peaks were observed at ~ 1.752 and ~ 1.728 eV, which are attributed to the neutral and charged exciton, respectively [2,6,33]. In fact, the delocalized exciton emission peak LX_0 from the defect site in single layer (Fig. 3) is significantly quenched in the presence of the localized exciton and is dominated by the redshifted emission from defects [2,33,35]. The PL line LX_0 , which coincides spectrally with the free exciton, is calculated in the presence of the random disorder potential $V(R)$. However, in contrast to the free exciton, which is characterized by a plane-wave function, LX_0 has an extended wave function on the whole crystal due to the disorder. It might be attributed to exciton states located at the mobility edge of the disordered 2D crystal, like in inhomogeneous semiconductor quantum wells. We expect thus that disorder acts as exciton traps and reduces the exciton mobility and diffusion length [84]. Moreover, one immediately notices that the sharp emission peaks originating from localized excitons LX_j ($j \geq 1$) are characterized by the superposition of an anharmonic spectrum. Comparing with the delocalized exciton emission in monolayer WSe₂, these localized emitters

have line-widths almost an order of magnitude sharper than the delocalized excitons in experimental situations [33–35]. In our calculation, the radiative damping of the localized states is much smaller than the intrinsic radiative damping of free excitons (of the order of 1–2 meV). From Figs. 3(a)–3(c), we notice that because of the variation of the correlation length L , the PLs spectra are significantly different from one simulation to another. In order to exhibit the effect of L , we consider the realization II as a reference and we compare it with the two other simulations. We start the discussion with simulation II [Fig. 3(b)], which corresponds to $L = 150 \text{ \AA}$. We notice that the spectrally localized emissions are located within the energy range 1.64–1.71 eV, which is lower than the PL line of the neutral exciton peak of WSe₂ (1.752 eV). The lowest line is located about 107 meV below the PL peak of the free neutral exciton. Comparing these results with the PL spectra illustrated in Figs. 3(a) and 3(c) and associated to the simulations I and III, respectively, we see that for localized states the spectral signature changes completely. We notice in particular that the energy shift between the free and the ground localized exciton $\Delta E = E_{X_0} - E_{LX_1}$ is strongly modified. In the simulation I, which corresponds to $L = 70 \text{ \AA}$ in Fig. 3(a), these defects introduce a narrow spectrum, located around 1.712 and 1.716 eV. These states correspond to the shallower localized exciton states. While for the realization III plotted in Fig. 3(c), the defects introduce a broad spectral region where localized exciton peaks appear, here between 1.54–1.7 eV. From this plot, we notice that the energy shift between the lowest localized exciton and the delocalized exciton increases by 113 meV when L increases from 150 to 600 \AA . Therefore we conclude that the exciton localization energy generally decrease when the local well extension increases.

E. Effect of the correlation length L on the radiative lifetime of the localized exciton

For most optoelectronic applications or possible realization of single photon source [2,35], knowing the radiative lifetimes of elementary excitations is critical [6,61–68]. To explore the effect of the three-dimensional quantum confinement of excitons, we now proceed to study the effect of L on the radiative lifetime of the localized exciton for the three different simulations by using the relation $\tau_{(j)}^{\text{rad}} = \frac{1}{p_{(j)}}$ and by comparing this result with the radiative lifetime of the free exciton. For light propagating perpendicular to the 2D layer and by assuming conservation of the in-plane wave vector, the radiative lifetime of the free exciton can be calculated using the expression given in the reference [67]. Thus we find a fast free exciton radiative lifetime on the order of 1 ps, this short lifetime being explained by strong confinement perpendicular to the monolayer, small exciton Bohr radius, and low average dielectric constant of the environment in WSe₂ monolayers [61]. However, as shown in Figs. 3(d)–3(f), for localized excitons, we calculate radiative lifetime much longer than the free exciton one: it varies from tens of picoseconds (for $L \sim R_{\text{cm}}$) to more than one nanosecond, becoming longer for larger values of correlation length L (i.e., for $L \gg R_{\text{cm}}$) [6,61]. The calculated lifetimes for the chosen values of R_{cm} and V_0 are quantitatively different from one simulation to another. As a matter of fact, when L is of the order of R_{cm} , i.e., for a narrow

well, the radiative lifetime is in the order of ten ps ($\tau_{(1)}^{\text{rad}} = 22 \text{ ps}$ for $L = 70 \text{ \AA}$) while the radiative lifetime can exceed one nanosecond for larger correlation lengths of the potential ($L \gg R_{\text{cm}}$), or strong disorder, which compares, e.g., to the experimental situation of Ref. [35]. We can conclude from these data that at low temperature, the increase of the local well extension leads to radiative lifetime considerably longer than the intrinsic radiative lifetime of the free exciton. We note also that the different values in each simulation are due to the complex potential landscape with localization sites of widely varying depth for excitons.

IV. IMPACT OF THE RANDOM POTENTIAL FLUCTUATION AMPLITUDE ON THE EXCITON STATES

To understand more deeply the localized states, we now turn to study the effect of the fluctuations amplitude (V_0) on the PL peaks spectral position and on the order of magnitude of localized exciton radiative lifetime in WSe₂. Different types of disorder potentials and their effects on excitonic properties are illustrated in Figs. 4(a) and 4(b) for a fixed value of $\frac{L}{R_{\text{cm}}} \sim 3$, and various amplitude values $V_0 = 2\hbar\omega_{\text{cm}}$, $11\hbar\omega_{\text{cm}}$, and $20\hbar\omega_{\text{cm}}$, with $\hbar\omega_{\text{cm}} = 10 \text{ meV}$.

According to the plots in the inset of Fig. 4(a), we notice that for fixed value of $L = 90 \text{ \AA}$, the depth of the disorder potential increases with the increase of V_0 , leading to the enhancement of the three-dimensional quantum confinement effects and consequently more localized excitonic states. This is observed by (i) the increase in the shift between the peaks of the localized exciton in a disorder potential and the peak of the free exciton ($E_{X_0} - E_{LX_1}$). (ii) The enhancement of the radiative lifetime of the localized exciton. In fact, it appears that at low temperature, for V_0 of the order of $\hbar\omega_{\text{cm}}$ ($V_0 \sim \hbar\omega_{\text{cm}}$), the exciton radiative lifetime is very small, in the order of ten picoseconds ($\tau_j^{\text{rad}} = 9\text{--}12 \text{ ps}$), only one order of magnitude longer than the free exciton one [54]. Such short radiative lifetimes are attributed to excitons weakly localized by a shallow potential [38]. Their spectral position

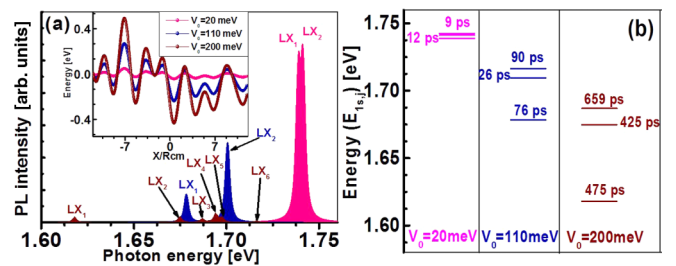


FIG. 4. (a) PL spectra of a WSe₂ monolayer for different values of V_0 (20 meV (pink), 110 meV (blue), and 200 meV (brown)) and for fixed $L = 90 \text{ \AA}$, $R_{\text{cm}} = 30 \text{ \AA}$, $N = 1000$, and a given realization of the random variables (θ_i , ϕ_i). The broadening parameter is set arbitrarily to $\gamma = 1 \text{ meV}$. The PL intensity is taken proportional to $P_{(j)}$. The inset displays the spatial variation of the random potential in the OX direction. (b) The energies of the localized exciton obtained by the numerical diagonalization of the matrix resulting from the projection of the Hamiltonian H and the corresponding radiative lifetime for the three first states for each random potential amplitude V_0 . The monolayer WSe₂ is deposited on the SiO₂/Si substrate and exposed to the air.

is only slightly redshifted compared to the delocalized states [$E_{X_0} - E_{LX_1} = 13$ meV on Fig. 4(b)]. For a large sample surface, this leads to inhomogeneous broadening of the free exciton resonance (still with a homogeneous contribution, however) and the possible appearance of a density of states tail. Nevertheless, from Figs. 4(a) and 4(b), we can notice that, for $V_0 = 200$ meV, the PL is strongly redshifted comparing to the first case ($V_0 = 20$ meV) and the ground state is located at 134 meV below the free exciton emission peak and we obtain a long radiative lifetime $\tau_1^{\text{rad}} = 475$ ps. We conclude that, for $V_0 \gg \hbar\omega_{\text{cm}}$, localized excitons exhibit long lifetime in the range of hundreds of picoseconds. These lifetimes can be two or three orders of magnitude longer than those of 2D free excitons in pristine monolayer WSe₂. This type of strongly localized exciton has been recently investigated in WSe₂ through single photon emission experiments [34,35,58]. In addition, Figs. 4(a) and 4(b) show also the increase of the spacing between the energy levels from 2.68 to 57 meV when the fluctuation amplitude increases from $V_0 = 20$ to 200 meV.

V. EFFECT OF THE DIELECTRIC ENVIRONMENT ON THE RADIATIVE LIFETIME

Because excitons in 2D semiconductors necessarily reside near a surface, their fundamental properties (size, binding energy, oscillator strength, radiative lifetime) are expected to be strongly influenced by any additional screening from the dielectric environment surrounding the monolayer [10,11]. After having studied in a previous work the effect of dielectric environment on the free exciton binding energy and PL emission spectrum [69], we now explore its impact on localized excitons spectrum and radiative lifetime. To this aim, we successively compare the case of a suspended monolayer in vacuum to an encapsulated hexagonal boron nitride (hBN), or to the cases of a monolayer deposited on silicon nitride (Si₃N₄) or on silicon dioxide (SiO₂) substrates. We study here specifically the dielectric environment influence on a WSe₂ monolayer at low temperature and for fixed values of the potential fluctuation amplitude ($V_0 = 110$ meV), correlation length ($L = 90$ Å), and using $R_{\text{cm}} = 30$ Å for the auxiliary basis.

As shown in Table I, it is clear that the radiative lifetime of the localized excitons is strongly sensitive to the dielectric environment and the choice of substrate material. Here, the

TABLE I. The influence of the dielectric environment on the radiative lifetime of localized exciton state LX_1 of WSe₂ monolayer in different cases: exposed to the air, or hBN encapsulated; deposited on different substrates: silicon nitride or SiO₂. κ is the average dielectric constant of the surrounding material. The fluctuation amplitude and correlation length of the disordered potential values are fixed to $V_0 = 110$ meV and $L = 90$ Å, respectively (the auxiliary basis parameter is set to $R_{\text{cm}} = 30$ Å).

| | encapsulated monolayer | supported monolayer | suspended monolayer | |
|----------------------------------|------------------------|--------------------------------|---------------------|--------|
| substrate | hBN | Si ₃ N ₄ | SiO ₂ | vacuum |
| dielectric constant ϵ_b | 4.5 | 7 | 3.9 | 1 |
| κ | 4.5 | 4 | 2.45 | 1 |
| radiative lifetime | 350 ps | 288 ps | 76 ps | 4ps |

role of the dielectric environment is captured by $\kappa = \frac{\epsilon_b + \epsilon_l}{2}$, the average dielectric constant of the surrounding material [69]. In fact, an obvious decrease of the radiative lifetime is observed due to the change of the average dielectric environment constant κ , going from encapsulated in hBN to suspended monolayer. It is noteworthy that without environmental screening (suspended monolayer) the lifetime of LX_1 state is 4 ps, while it rises to 76 ps when deposited on a SiO₂ substrate ($\kappa = 2.45$), and reaches 350 ps when the monolayer is encapsulated in between the hBN flakes, $\kappa = 4.5$. This change in the magnitude order of the radiative lifetime with the dielectric environment can be explained by the reduced spatial overlap between the electron and the hole in their relative motion [12] due to the increase of the dielectric screening, resulting in the decrease of the oscillator strength when the dielectric screening increases and hence in longer radiative lifetimes.

VI. COMPARISON WITH THE EXPERIMENT

Understanding the effect of each parameter of the disorder potential, allows us to control our model in order to reproduce the experimental observations. In this section, we will calculate the energy and the radiative lifetime of neutral excitons localized at a local minimum of the random potential. According to Ref. [6], we address typically the situation where the WSe₂ monolayer samples are micromechanically cleaved from a bulk WSe₂ crystal and deposited on a SiO₂ layer on top of a Si substrate. The fluctuations of the local charge distribution, and structural random defects of SiO₂ as well as surface roughness of the latter may induce here the potential fluctuations modelled in this work. Besides, we recall that we assume low-doping density, weak excitation conditions avoiding efficient photodoping as well as biexciton generation, and low temperature conditions (here $T = 4$ K), where the low-energy lines are present (these lines usually disappear above 150 K typically [6]). Finally, we neglect here the optical interferences, which may arise depending on the SiO₂ layer thickness, and modify the radiative lifetime [85].

Our objective is to check the validity of our model by a comparison between the radiative lifetimes calculated in our model and those observed in Ref. [6]. As we said previously, the fluctuations of the crystal potential are governed by the parameters (V_0, L). In order to reproduce the observed energy positions of the different localized states, we have found that the following set of parameters $N = 1000$, $V_0 = 110$ meV, and $L = 90$ Å [the blue data in Figs. 4(a) and 4(b)] gives results in good agreement with the experiment of Ref. [6] (we have taken here for the auxiliary basis $\hbar\omega_{\text{cm}} = 10$ meV). In this work, the time-resolved measurements of spontaneous emission gave the localized exciton overall decay times. However, our model calculates only the radiative ones. In fact, the experimental decay time is defined as $\frac{1}{\tau_{\text{decay}}} = \frac{1}{\tau^{\text{rad}}} + \frac{1}{\tau^{\text{nrad}}}$, where τ^{nrad} is the nonradiative lifetime due to possible nonradiative recombination channels. In the following, we shall assume that, due to the strong exciton localization and low diffusion rate at low temperature [86], the nonradiative recombination rate is negligible as compared to the radiative recombination rate $P_{(j)}^{\text{rad}} \gg P_{(j)}^{\text{nrad}}$, therefore $\tau_{\text{decay}} \sim \tau^{\text{rad}}$. Using our model, we found that for the peak labeled LX_2

located at 1.7 eV, the radiative lifetime calculated here is about $\tau_{(2)}^{\text{rad}} = 26$ ps. The peak LX_1 located at 1.678 eV has a significantly longer radiative lifetime of $\tau_{(1)}^{\text{rad}} = 76$ ps [the blue data in Figs. 4(a) and 4(b)]. This is in reasonable agreement with the experimental data $\tau_{(1)}^{\text{exp}} = 80 \pm 6$ ps (LX_1 line) and $\tau_{(1)}^{\text{exp}} = 32 \pm 2$ (LX_2 line) [87]. This means that our set of disorder parameters can reproduce reasonably well both the experimentally observed localized exciton spectral position and decay times, and that our theory supports the identification of the low-energy lines LX_1 and LX_2 as due to localized exciton states. We note that the LX_3 line predicted by the model at 1.72 eV were not observed experimentally, probably due to the inhomogeneous broadening of the nearby trion line.

VII. CONCLUSION

In summary, localized excitons in monolayer WSe_2 are described within the Wannier-Mott exciton model in which we have described the structural imperfections, which may arise due to lattice structural defects, residual impurities, and adatoms commonly introduced during the mechanical exfoliation process via a random disorder potential. We have studied the effect of the characteristic parameters (spatial fluctuations in amplitude, correlation length) of the disorder potential on the excitonic properties. We have theoretically investigated the evolution of multiple PL emission peaks in monolayer WSe_2 as well as their associated energies, wave functions, and radiative lifetime at low temperature (4 K) and low excitation density. We have proved that the disorder potential arising from defects strongly affects the exciton states, which can lead either to inhomogeneous broadening of the exciton resonance and the appearance of a density of localized state tail or the appearance of more deeply localized states, depending on the values of the disorder parameters. We have demonstrated that, compared to the free excitons, excitons trapped in potential wells present a significant enhancement of their radiative lifetime. We proved that the exciton radiative lifetime strongly depends not only on the disorder parameters but also on the dielectric screening. We found that if the exciton is weakly localized, i.e., in the case when $L \sim R_{\text{cm}}$ or/and $V_0 \sim \hbar\omega_{\text{cm}}$ (narrow and shallow well), the radiative lifetime is of the order of tens of picosecond, while it ranges from hundreds of picoseconds to few nanoseconds when $L \gg R_{\text{cm}}$ or/and $V_0 \gg \hbar\omega_{\text{cm}}$, i.e., for larger and deeper wells. Finally, in order to validate our model, we compare our results with the experiment presented in Ref. [6] taken as an example. The good agreement obtained supports our interpretation of the low-energy lines in terms of localized excitons in a disorder potential.

The theory presented here could, in principle, be applied to any monolayer tungstenide or molybdenide TMDs 2D crystals. However, it could only be checked in tungstenides where, by contrast with molybdenides, the localized exciton lines are currently observed.

APPENDIX A: RANDOM POTENTIAL CALCULATION

The potential $V(\mathbf{R})$ is taken as a Gaussian random field with zero-mean V_0 variance and correlation length L . In the following, we describe the construction of this potential and we verify it has suitable properties. To achieve this, the potential

function $V(\mathbf{R})$ is modelled by the superposition of N random plane waves with random direction θ_j , random phase ϕ_j , and constant wavelength L . Letting the phase at the point $(0,0)$ be ϕ_j , the potential is then given by

$$\begin{aligned} V(\mathbf{R}) &= C\sqrt{N}V_0 \sum_{j=1}^N \Re\{e^{i(\mathbf{K}(\theta_j)\cdot\mathbf{R}+\phi_j)}\} \\ &= C'V_0 \sum_{j=1}^N \cos\{\mathbf{K}(\theta_j)\cdot\mathbf{R} + \phi_j\} \end{aligned} \quad (\text{A1})$$

with $V_0 > 0$ and $C' = C\sqrt{N}$, where the constant C will be defined later. The random variables θ_j and ϕ_j are both uniformly distributed on $[0, 2\pi]$ and are uncorrelated so we can consider that $j = (k, l)$ with $k_{\text{max}}l_{\text{max}} = N$. Letting $\mathbf{K}(\theta_j) = \frac{2\pi}{L}\mathbf{U}(\theta_j)$, with $\mathbf{U}(\theta_j) = (\cos\theta_j, \sin\theta_j)$, we introduce the dimensionless position $\mathbf{R}' = \frac{2\pi}{L}\mathbf{R}$ and potential $V'(\mathbf{R}') = \frac{V(\mathbf{R})}{V_0}$. The normalized potential can thus be rewritten as

$$V'(\mathbf{R}') = \frac{C'}{2} \sum_{k=1}^{k_{\text{max}}} \sum_{l=1}^{l_{\text{max}}} \{e^{i(\mathbf{u}(\theta_k)\cdot\mathbf{R}'+\phi_l)} + e^{-i(\mathbf{u}(\theta_k)\cdot\mathbf{R}'+\phi_l)}\}. \quad (\text{A2})$$

If N is sufficiently large, then $V'(\mathbf{R}')$ is a large sum of random variables and by the central limit theorem, $V'(\mathbf{R}')$ is Gaussian.

1. Mean value of the disorder potential $V'(\mathbf{R}')$

The mean value of the normalized potential $V'(\mathbf{R}')$ over all random variables is written as

$$\langle \overline{V'(\mathbf{R}')} \rangle = \frac{C'}{2N} \sum_{k=1}^{k_{\text{max}}} \sum_{l=1}^{l_{\text{max}}} \{e^{i(\mathbf{u}(\theta_k)\cdot\mathbf{R}'+\phi_l)} + e^{-i(\mathbf{u}(\theta_k)\cdot\mathbf{R}'+\phi_l)}\}. \quad (\text{A3})$$

Note that since $\theta, \phi \in [0, 2\pi]$, their probability distribution functions are $f_1(\theta) = \frac{1}{2\pi}$ and $f_2(\phi) = \frac{1}{2\pi}$ and

$$\begin{aligned} \langle \overline{V'(\mathbf{R}')} \rangle_{N \rightarrow \infty} &= \frac{C'}{2} \int_0^{2\pi} e^{i\mathbf{u}(\theta)\cdot\mathbf{R}'} \frac{d\theta}{2\pi} \int_0^{2\pi} e^{i\phi} \frac{d\phi}{2\pi} + \text{c.c.} \\ &= 0 \end{aligned} \quad (\text{A4})$$

2. Variance of the disorder potential $V'(\mathbf{R}')$

Since the potential has zero mean $\langle \overline{V'(\mathbf{R}')} \rangle = 0$, the variance of the normalized potential reduces to $\sigma_{V'}^2 = \langle \overline{V'^2(\mathbf{R}')} \rangle$. It is calculated as

$$\begin{aligned} \langle \overline{V'^2(\mathbf{R}')} \rangle &= \frac{C'^2}{4N} \left\{ \sum_{k=1}^{k_{\text{max}}} \sum_{l=1}^{l_{\text{max}}} (e^{i(\mathbf{u}(\theta_k)\cdot\mathbf{R}'+\phi_l)} + e^{-i(\mathbf{u}(\theta_k)\cdot\mathbf{R}'+\phi_l)}) \right\}^2 \\ &= \frac{C'^2}{4N} \left\{ \sum_{k,l}^{k_{\text{max}},l_{\text{max}}} [2 + e^{2i(\mathbf{u}(\theta_k)\cdot\mathbf{R}'+\phi_l)} + e^{-2i(\mathbf{u}(\theta_k)\cdot\mathbf{R}'+\phi_l)}] \right. \\ &\quad + \sum_{(k,l) \neq (k',l')} [e^{i(\mathbf{u}(\theta_k)\cdot\mathbf{R}'+\phi_l)} + e^{-i(\mathbf{u}(\theta_k)\cdot\mathbf{R}'+\phi_l)}] \\ &\quad \left. \times [e^{i(\mathbf{u}(\theta_{k'})\cdot\mathbf{R}'+\phi_{l'})} + e^{-i(\mathbf{u}(\theta_{k'})\cdot\mathbf{R}'+\phi_{l'})}] \right\}. \end{aligned} \quad (\text{A6})$$

Transforming as previously the discrete summation to integrals when $N \rightarrow \infty$, the variance $\sigma_{V'}^2$ is equivalent to

$$\overline{\langle V'^2(\mathbf{R}') \rangle}_{N \rightarrow \infty} \sim \frac{C'^2}{2}. \quad (\text{A7})$$

The condition $\sigma_V^2 = V_0^2$ implies $\sigma_{V'}^2 = 1$, which determines C' . We get $C' = \sqrt{2}$ as a normalization constant. Note that $\sigma_{V'}$ is independent of the position \mathbf{R}' . Finally, the random disorder potential is rewritten as

$$\begin{aligned} V'(\mathbf{R}') &= \sqrt{\frac{2}{N}} \sum_{j=1}^N \cos[\mathbf{u}(\theta_j) \cdot \mathbf{R}' + \phi_j] \\ &= \sqrt{\frac{2}{N}} \sum_{j=1}^N \cos[|\mathbf{R}'| \cos(\theta_j - \varphi_{R'}) + \phi_j] \end{aligned} \quad (\text{A8})$$

with $\mathbf{R}' = |\mathbf{R}'|(\cos \varphi_{R'}, \sin \varphi_{R'})$. It follows that the expression of the initial random disorder potential is given by

$$V(\mathbf{R}) = \sqrt{\frac{2}{N}} V_0 \sum_{j=1}^N \cos \left[\frac{2\pi}{L} |\mathbf{R}| \cos(\theta_j - \varphi_R) + \phi_j \right]. \quad (\text{A9})$$

As demonstrated, this potential has zero mean $\overline{\langle V(\mathbf{R}) \rangle} = 0$ and constant standard deviation equal to $\sigma_V = \overline{\langle V^2(\mathbf{R}) \rangle}^{\frac{1}{2}} = V_0$. We note that the disorder potential $V(\mathbf{R})$ has no spa-

tial periodicity. Each space wave j has a random period of $|\Delta \mathbf{R}_j| = \frac{L}{\cos(\theta_j - \varphi_R)}$. Only the waves propagating exactly in the direction of \mathbf{R} are periodic with translations with a multiple of the wavelength L . The distribution, height, depth, and the form of the potential are different from one simulation to another.

3. Calculation of the correlation length of the disorder potential $V(\mathbf{R})$

The correlation length is given by the expression

$$C(R_1, R_2) = \frac{\overline{\langle V(\mathbf{R}_1)V(\mathbf{R}_2) \rangle} - \overline{\langle V(\mathbf{R}_1) \rangle} \overline{\langle V(\mathbf{R}_2) \rangle}}{\overline{\langle V^2(\mathbf{R}_1) \rangle}^{\frac{1}{2}} \overline{\langle V^2(\mathbf{R}_2) \rangle}^{\frac{1}{2}}}. \quad (\text{A10})$$

In the previous section, we demonstrated that $\overline{\langle V'(\mathbf{R}'_1) \rangle} = \overline{\langle V'(\mathbf{R}'_2) \rangle} = 0$ and $\overline{\langle V'^2(\mathbf{R}'_1) \rangle} = \overline{\langle V'^2(\mathbf{R}'_2) \rangle} = 1$. So the spatial correlation function of the normalized potential between \mathbf{R}'_1 and \mathbf{R}'_2 points can be written as

$$C'(\mathbf{R}'_1, \mathbf{R}'_2) = C \left(\frac{L}{2\pi} \mathbf{R}'_1, \frac{L}{2\pi} \mathbf{R}'_2 \right) = \overline{\langle V'(\mathbf{R}'_1)V'(\mathbf{R}'_2) \rangle}. \quad (\text{A11})$$

We calculate first

$$\begin{aligned} V'(\mathbf{R}'_1)V'(\mathbf{R}'_2) &= \frac{1}{2} \sum_{k,l}^{k_{\max}, l_{\max}} \sum_{k',l'=1}^{k_{\max}, l_{\max}} [e^{i(\mathbf{u}(\theta_k)\mathbf{R}'_1 + \phi_k)} + e^{-i(\mathbf{u}(\theta_k)\mathbf{R}'_1 + \phi_k)}][e^{i(\mathbf{u}(\theta_{k'})\mathbf{R}'_2 + \phi_{k'})} e^{i(\mathbf{u}(\theta_{l'})\mathbf{R}'_2 + \phi_{l'})}] \\ &= \frac{1}{2} \sum_{k,l}^{k_{\max}, l_{\max}} \{e^{i(\mathbf{u}(\theta_k) \cdot (\mathbf{R}'_1 - \mathbf{R}'_2))} + \text{c.c.}\} + \sum_{k,l}^{k_{\max}, l_{\max}} \sum_{(k',l') \neq (k,l)}^{k_{\max}, l_{\max}} \{e^{i(\mathbf{u}(\theta_k) \cdot \mathbf{R}'_1 - \mathbf{u}(\theta_{k'}) \cdot \mathbf{R}'_2 + \phi_l - \phi_{l'})} + \text{c.c.}\} \\ &\quad + \frac{1}{2} \sum_{k,l}^{k_{\max}, l_{\max}} \sum_{k',l'=1}^{k_{\max}, l_{\max}} e^{i(\mathbf{u}(\theta_k) \cdot \mathbf{R}'_1 - \mathbf{u}(\theta_{k'}) \cdot \mathbf{R}'_2 + \phi_l - \phi_{l'})} + \text{c.c.} \end{aligned} \quad (\text{A12})$$

In the limit when N is sufficiently large the second and the third summation will give a zero contribution, hence

$$C'(\mathbf{R}'_1, \mathbf{R}'_2)_{N \rightarrow \infty} \sim \frac{1}{2} \int_0^{2\pi} \frac{d\theta}{2\pi} \frac{d\phi}{2\pi} (e^{i(\mathbf{u}(\theta_k) \cdot (\mathbf{R}'_1 - \mathbf{R}'_2))} + \text{c.c.}) = \int_0^{2\pi} \frac{d\theta}{2\pi} \cos [|\mathbf{R}'_1 - \mathbf{R}'_2| \cos(\theta_k - \varphi_{R'_1 - R'_2})]. \quad (\text{A13})$$

Here, $\mathbf{R}'_1 - \mathbf{R}'_2 = |\mathbf{R}'_1 - \mathbf{R}'_2|(\cos(\varphi_{R'_1 - R'_2}), \sin(\varphi_{R'_1 - R'_2}))$. In normalized units, we arrive to

$$C'(\mathbf{R}'_1, \mathbf{R}'_2) = J_0(|\mathbf{R}'_1 - \mathbf{R}'_2|) \quad (\text{A14})$$

and we get finally for the spatial correlation function the expression

$$C(\mathbf{R}_1, \mathbf{R}_2) = J_0 \left(\frac{2\pi}{L} |\mathbf{R}_1 - \mathbf{R}_2| \right). \quad (\text{A15})$$

Note that $C(\mathbf{R}_1, \mathbf{R}_2)$ tend to 1 when $|\mathbf{R}_1 - \mathbf{R}_2| \rightarrow 0$. From Eq. (A 15) and the properties of the Bessel function, we see the correlation function is quasiperiodic with respect to $|\mathbf{R}_1 - \mathbf{R}_2|$ as soon as $|\mathbf{R}_1 - \mathbf{R}_2| \geq L$, with a pseudoperiod roughly equal to L . This appears clearly in Fig. 5 where the successive maxima (minima) appear quasi-periodically

with respect to L . It can also be seen from expression (A15) that the correlation function decays with a typical length of about L .

APPENDIX B: SCALING PROPERTIES

1. Choice of the basis

In our theory, the choice of the basis is tightly linked to the behavior of the potential. As a fact, the basis of the harmonic function, which are Hermite polynomials multiplied by Gaussian functions $\{\xi_{n_x, n_y}; n_x, n_y \in \mathbb{N}\}$, is complete only in the case where the harmonic potential from which it derives is not superiorly bounded (i.e., in the infinite parabolic well case). Hence all the states are located in the well. In our case, the random potential fluctuations are bounded (basically,

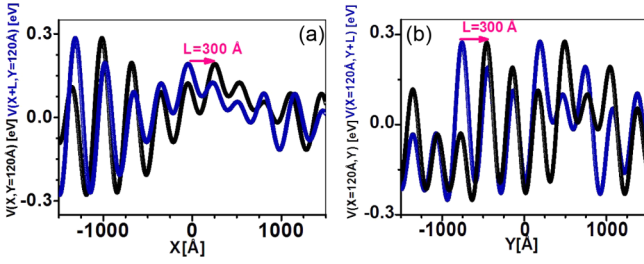


FIG. 5. (a) The variation of the disorder potential $V(X, Y = 120 \text{ \AA})$ (black) and $V(X + L, Y = 120 \text{ \AA})$ (blue) as a function of center of mass coordinate X and for $Y = 120 \text{ \AA}$. (b) The variation of the disorder potential $V(X = 120 \text{ \AA}, Y)$ and $V(X = 120 \text{ \AA}, Y + L)$ as a function of center of mass coordinate Y and for $X = 120 \text{ \AA}$. The parameters used are $V_0 = 110 \text{ meV}$, $R_{\text{cm}} = 30 \text{ \AA}$, and $L = 300 \text{ \AA}$.

the potential is limited by its typical amplitude fluctuations $\pm\sigma_V = \pm V_0$). The general solution, compatible with the behavior of our potential, should be written using the two orthogonal parabolic cylinder functions of first and second kind. These functions are the solutions of the generic second-order differential equation $-y''[X] + (\frac{X^2}{4} - \nu - \frac{1}{2})y[X] = 0$. The general solution thus writes

$$y[X] = c_1 2^{-\frac{\nu}{2}} e^{-\frac{X^2}{4}} \mathbf{H}_\nu \left[\frac{X}{\sqrt{2}} \right] + c_2 2^{\frac{1+\nu}{2}} e^{\frac{X^2}{4}} \mathbf{H}_{-1-\nu} \left[\frac{iX}{\sqrt{2}} \right] \\ = c_1 b_{1,\nu}(X) + c_2 b_{2,\nu}(X), \quad (\text{B1})$$

$$\langle \xi_{n_x, n_y}(X, Y) | \frac{P^2}{2M_X} | \xi_{n'_x, n'_y}(X, Y) \rangle = \frac{\hbar\omega_{\text{cm}}}{4} T(n_x, n_y, n'_x, n'_y). \quad (\text{B3})$$

Here,

$$T(n_x, n_y, n'_x, n'_y) = [(2n_x + 1)\delta_{n_x, n'_x} - \sqrt{n_x(n_x - 1)}\delta_{n_x, n'_x - 2} - \sqrt{(n_x + 2)(n_x + 1)}\delta_{n_x, n'_x + 2}] \delta_{n_y, n'_y} \\ + [(2n_y + 1)\delta_{n_y, n'_y} - \sqrt{n_y(n_y - 1)}\delta_{n_y, n'_y - 2} - \sqrt{(n_y + 2)(n_y + 1)}\delta_{n_y, n'_y + 2}] \delta_{n_x, n'_x}. \quad (\text{B4})$$

Note that the kinetic energy term at the matrix element is independent from the disorder potential.

(ii) The potential energy contribution to the matrix elements is in turn given by

$$\langle \xi_{n_x, n_y}(X, Y) | V(X, Y) | \xi_{n'_x, n'_y}(X, Y) \rangle = \frac{\sqrt{2}V_0}{\sqrt{N\pi}R_{\text{cm}}^2} \frac{1}{\sqrt{2^{n_x, n_y, n'_x, n'_y}}} \times \frac{1}{\sqrt{n_x! n_y! n'_x! n'_y!}} \sum_{j=1}^N \iint_{-\infty}^{+\infty} dXdY \mathbf{H}_{n_x} \left(\frac{X}{R_{\text{cm}}} \right) \\ \times \mathbf{H}_{n'_x} \left(\frac{X}{R_{\text{cm}}} \right) \mathbf{H}_{n_y} \left(\frac{Y}{R_{\text{cm}}} \right) \mathbf{H}_{n'_y} \left(\frac{Y}{R_{\text{cm}}} \right) e^{-\frac{X^2}{R_{\text{cm}}^2}} e^{-\frac{Y^2}{R_{\text{cm}}^2}} \cos \left[\frac{2\pi}{L} X \cos(\theta_j) + \frac{2\pi}{L} Y \sin(\theta_j) + \phi_j \right]. \quad (\text{B5})$$

The kinetic contribution in the equation being known, therefore the whole problem is to evaluate the matrix element, which contains the potential energy. This term is at the origin of the impact of the disorder potential on the exciton center of mass (COM) spectral properties. The exciton COM problem defined by the Hamiltonian (2) in the main text and the random disorder potential (4) depends on two independent parameters, the correlation length L and the amplitude fluctuations potential V_0 . Taking the auxiliary basis ξ_{n_x, n_y} , a third parameter appears which is the energy quantum $\hbar\omega_{\text{cm}}$; the corresponding localization length is $R_{\text{cm}} = \sqrt{\frac{\hbar}{M_X \omega_{\text{cm}}}}$. These quantities will be taken as energy and length units in the following. Let us introduce the dimensionless coordinates $X' = \frac{X}{R_{\text{cm}}}$, $Y' = \frac{Y}{R_{\text{cm}}}$. Dividing the matrix element by $\hbar\omega_{\text{cm}}$ and letting $\alpha_j = 2\pi \frac{R_{\text{cm}}}{L} \cos(\theta_j)$ and $\beta_j = 2\pi \frac{R_{\text{cm}}}{L} \sin(\theta_j)$,

where c_1 and c_2 are arbitrary constants. The first term is identified with the eigenfunctions of the harmonic oscillator and is always normalizable:

$$\xi_n[X] = \frac{\mathbf{H}_n[X] e^{-\frac{X^2}{2}}}{\sqrt{2^n n!} \sqrt{\pi}}. \quad (\text{B2})$$

However, the second function is necessary in the case where there is a truncated harmonic well (as in the usual case of a finite square quantum well) or more generally superiorly bounded (another generic solution of Schrödinger equation should then be found out of the domains where the potential is considered as harmonic). Since we restrict here to the case where the excitons are confined in the local wells of the sample, i.e., the energy levels are small compared to the potential fluctuations, we can neglect the contributions of the second function $b_{2,\nu}(X)$ and restrict our function basis to the first one, $b_{1,\nu}(X)$. The validity condition of the eigensolution of energy E_n is thus given by $E_n \ll V_0$ ($n = 1, 2, \dots$). Hence the choice of this basis is only valid in the case when $\hbar\omega_{\text{cm}} < V_0$.

After the choice of the basis, we analyze now the situation where the disorder induced by defects of the monolayer 2D crystal affects only the center of mass motion. In this case, the matrix elements of the center of mass Hamiltonian are the sum of two contributions: (i) the kinetic energy contribution to the matrix elements in Eq. (7) is given by

we get

$$\begin{aligned} \langle \xi_{n_x, n_y} | \tilde{H}_{\text{cm}} | \xi_{n'_x, n'_y} \rangle &= \langle \tilde{E}_c \rangle_{n_x, n_y, n'_x, n'_y} + \langle \tilde{E}_p \rangle_{n_x, n_y, n'_x, n'_y} \\ &= \frac{1}{4} T(n_x, n_y, n'_x, n'_y) + \frac{V_0}{\hbar \omega_{\text{cm}}} A_{n_x, n_y, n'_x, n'_y} e^{-\left(\frac{\pi R_{\text{cm}}}{L}\right)^2} \sum_{j=1}^N \mathcal{F}(n_x, n_y, n'_x, n'_y, \alpha_j, \beta_j). \end{aligned} \quad (\text{B6})$$

Here,

$$A_{(n_x, n_y, n'_x, n'_y)} = \frac{(-1)^{n_x + n_y}}{\sqrt{N}} \sqrt{\frac{2^{n_x + n_y + \frac{1}{2}} n_x! n_y!}{2^{n'_x + n'_y} n'_x! n'_y!}} \quad (\text{B7})$$

and

$$\mathcal{F}(n_x, n_y, n'_x, n'_y, \alpha_j, \beta_j) = \cos \phi_j \wp(n_x, n_y, n'_x, n'_y, \alpha_j, \beta_j) - \sin \phi_j \aleph(n_x, n_y, n'_x, n'_y, \alpha_j, \beta_j) \quad (\text{B8})$$

with

$$\begin{aligned} \wp(n_x, n_y, n'_x, n'_y, \alpha_j, \beta_j) &= \alpha_j^{2|m_x|} \beta_j^{2|m_y|} L_{n_x}^{2|m_x|} \left(\frac{\alpha_j^2}{2}\right) L_{n_y}^{2|m_y|} \left(\frac{\beta_j^2}{2}\right) \delta_{n'_x, n_x + 2m_x} \delta_{n'_y, n_y + 2m_y} - \alpha_j^{2|m_x|+1} \beta_j^{2|m_y|+1} L_{n_x}^{2|m_x|+1} \left(\frac{\alpha_j^2}{2}\right) \\ &\quad \times L_{n_y}^{2|m_y|+1} \left(\frac{\beta_j^2}{2}\right) \delta_{n'_x, n_x + 2m_x + 1} \delta_{n'_y, n_y + 2m_y + 1}, \end{aligned} \quad (\text{B9})$$

$$\begin{aligned} \aleph(n_x, n_y, n'_x, n'_y, \alpha_j, \beta_j) &= \alpha_j^{2|m_x|+1} \beta_j^{2|m_y|} L_{n_x}^{2|m_x|+1} \left(\frac{\alpha_j^2}{2}\right) L_{n_y}^{2|m_y|} \left(\frac{\beta_j^2}{2}\right) \delta_{n'_x, n_x + 2m_x + 1} \delta_{n'_y, n_y + 2m_y} + \alpha_j^{2|m_x|} \beta_j^{2|m_y|+1} \\ &\quad \times L_{n_x}^{2|m_x|} \left(\frac{\alpha_j^2}{2}\right) \times L_{n_y}^{2|m_y|+1} \left(\frac{\beta_j^2}{2}\right) \delta_{n'_x, n_x + 2m_x} \delta_{n'_y, n_y + 2m_y + 1}. \end{aligned} \quad (\text{B10})$$

Here, \mathbf{H}_{n_i} ($i = x, y$) is the Hermite polynomials with $n_i \in \mathbb{N}$ being the quantum numbers, $L_{n_i}^\lambda(\zeta)$ is the associated orthogonal Laguerre polynomials, $m_i \in \mathbb{Z}$. In our work, we choose R_{cm} smaller than the correlation length ($R_{\text{cm}} < L$). Together with the condition $\hbar \omega_{\text{cm}} < V_0$ this ensures sufficient accuracy in the numerical calculation of the eigensolutions. We thus define $L = p R_{\text{cm}}$ ($p > 1$), and $V_0 = k \hbar \omega_{\text{cm}}$ (it is sufficient here to restrict to $k \in \mathbb{N}^*$). Finally, there are only two independent dimensionless parameters in the problem, namely, $\frac{V_0}{\hbar \omega_{\text{cm}}}$ and $\frac{L}{R_{\text{cm}}}$.

-
- [1] C. Janisch, Y. Wang, D. Ma, N. Mehta, A. L. Elías, N. Perea-López, M. Terrones, V. Crespi, and Z. Liu, *Sci. Rep.* **4**, 5530 (2014).
- [2] P. Tonndorf, R. Schmidt, R. Schneider, J. Kern, M. Buscema, G. A. Steele, A. Castellanos-Gomez, H. S. J. van der Zant, S. M. de Vasconcelos, and R. Bratschitsch, *Optica* **2**, 347 (2015).
- [3] B. Zhu, X. Chen, and X. Cui, *Sci. Rep.* **5**, 9218 (2015).
- [4] J. Huang, T. B. Hoang, and M. H. Mikkelsen, *Sci. Rep.* **6**, 22414 (2016).
- [5] A. T. Hanbicki, G. Kioseoglou, M. Currie, C. Stephen Hellberg, K. M. McCreary, A. L. Friedman, and B. T. Jonker, *Sci. Rep.* **6**, 18885 (2016).
- [6] G. Wang, L. Bouet, D. Lagarde, M. Vidal, A. Balocchi, T. Amand, X. Marie, and B. Urbaszek, *Phys. Rev. B* **90**, 075413 (2014).
- [7] K. F. Mak, C. Lee, J. Hone, J. Shan, and T. F. Heinz, *Phys. Rev. Lett.* **105**, 136805 (2010).
- [8] S. Zhang, C.-G. Wang, M.-Y. Li, D. Huang, L.-J. Li, W. Ji, and S. Wu, *Phys. Rev. Lett.* **119**, 046101 (2017).
- [9] D. K. Zhang, D. W. Kidd, and K. Varga, *Nano Lett.* **15**, 7002 (2015).
- [10] A. V. Stier, N. P. Wilson, G. Clark, X. Xu, and S. A. Crooker, *Nano Lett* **16**, 7054 (2016).
- [11] A. Raja, A. Chaves, J. Yu, G. Arefe, H. M. Hill, A. F. Rigosi, T. C. Berkelbach, P. Nagler, C. Schüller, T. Korn, C. Nuckolls, J. Hone, L. E. Brus, T. F. Heinz, D. R. Reichman, and A. Chernikov, *Nat Commun* **8**, 15251 (2017).
- [12] L. Cao, *MRS Bull.* **40**, 592 (2015).
- [13] T. Jakubczyk, K. Nogajewski, M. R. Molas, M. Bartos, W. Langbein, M. Potemski, and J. Kasprzak, *2D Mater.* **5**, 031007 (2018).
- [14] Y. Zhou, G. Scuri, D. S. Wild, A. A. High, A. Dibos, L. A. Jauregui, C. Shu, K. D. Greve, K. Pistunova, A. Y. Joe, T. Taniguchi, K. Watanabe, P. Kim, M. D. Lukin, and H. Park, *Nat. Nanotechnol.* **12**, 856 (2017).
- [15] C. Robert, T. Amand, F. Cadiz, D. Lagarde, E. Courtade, M. Manca, T. Taniguchi, K. Watanabe, B. Urbaszek, and X. Marie, *Phys. Rev. B* **96**, 155423 (2017).
- [16] M. M. Perera, M. W. Lin, H. J. Chuang, B. P. Chamlagain, C. Wang, X. Tan, M. M. C. Cheng, D. Tománek, and Z. Zhou, *ACS Nano* **7**, 4449 (2013).
- [17] H. Li, J. Wu, Z. Yin, and H. Zhang, *Acc. Chem. Res.* **47**, 1067 (2014).
- [18] S. Das, M. Dubey, and A. Roelofs, *Appl. Phys. Lett.* **105**, 083511 (2014).
- [19] M. S. Choi, D. Qu, D. Lee, X. Liu, K. Watanabe, T. Taniguchi, and W. Jong Yoo, *ACS Nano* **8**, 9332 (2014).

- [20] W. Yang, J. Shang, J. Wang, X. Shen, B. Cao, N. Peimyoo, C. Zou, Y. Chen, Y. Wang, C. Cong, W. Huang, and T. Yu, *Nano Lett.* **16**, 1560 (2016).
- [21] J. S. Ross, P. Klement, A. M. Jones, N. J. Ghimire, J. Yan, D. G. Mandrus, T. Taniguchi, K. Watanabe, K. Kitamura, W. Yao, D. H. Cobden, and X. Xu, *Nat. Nanotechnol.* **9**, 268 (2014).
- [22] M. H. Tahersima and V. J. Sorger, *Nanotechnology* **26**, 344005 (2015).
- [23] R. S. Sundaram, M. Engel, A. Lombardo, R. Krupke, A. C. Ferrari, Ph. Avouris, and M. Steiner, *Nano Lett.* **13**, 1416 (2013).
- [24] Y. Ye, Z. Ye, M. Gharghi, H. Zhu, M. Zhao, Y. Wang, X. Yin, and X. Zhang, *Appl. Phys. Lett.* **104**, 193508 (2014).
- [25] O. L. Sanchez, E. A. Llado, V. Koman, A. F. I. Morral, A. Radenovic, and A. Kis, *ACS Nano* **8**, 3042 (2014).
- [26] S. Wu, S. Buckley, J. R. Schaibley, L. Feng, J. Yan, D. G. Mandrus, F. Hatami, W. Yao, J. Vukovi, A. Majumdar, and X. Xu, *Nature (London)* **520**, 69 (2015).
- [27] Y. Ye, Z. J. Wong, X. Lu, X. Ni, H. Zhu, X. Chen, Y. Wang, and X. Zhang, *Nat. Photonics* **9**, 733 (2015).
- [28] Q. H. Wang, K. K. Zadeh, A. Kis, J. N. Coleman, and M. S. Strano, *Nat. Nanotechnol.* **7**, 699 (2012).
- [29] J. Lu, H. Liu, E. S. Toka, and C. H. Sow, *Chem. Soc. Rev.* **45**, 2494 (2016).
- [30] D. Xiao, G. B. Liu, W. Feng, X. Xu, and W. Yao, *Phys. Rev. Lett.* **108**, 196802 (2012).
- [31] A. Rycerz, J. Tworzydło, and C. W. J. Beenakker, *Nat. Phys.* **3**, 172 (2007).
- [32] Z. Zhu, A. Collaudin, B. Fauque, W. Kang, and K. Behnia, *Nat. Phys.* **8**, 89 (2012).
- [33] C. Chakraborty, K. M. Goodfellow, and A. N. Vamivakas, *Opt. Mater. Express* **6**, 2081 (2016).
- [34] Y. M. He, G. Clark, J. R. Schaibley, Y. He, M. C. Chen, Y. J. Wei, X. Ding, Q. Zhang, W. Yao, X. Xu, C. Yang Lu, and J. W. Pan, *Nat. Nanotechnol.* **10**, 497 (2015).
- [35] A. Srivastava, M. Sidler, A. V. Allain, D. S. Lembke, A. Kis, and A. Imamoglu, *Nat. Nanotechnol.* **10**, 491 (2015).
- [36] S. Schwarz, A. Kozikov, F. Withers, J. K. Maguire, A. P. Foster, S. Dufferwiel, L. Hague, M. N. Makhonin, L. R. Wilson, A. K. Geim, K. S. Novoselov, and A. I. Tartakovskii, *2D Mater.* **3**, 2053 (2016).
- [37] M. Koperski, K. Nogajewski, A. Arora, V. Cherkez, P. Mallet, J. Y. Veuillen, J. Marcus, P. Kossacki, and M. Potemski, *Nat. Nanotechnol.* **10**, 503 (2015).
- [38] F. Cadiz, E. Courtade, C. Robert, G. Wang, Y. Shen, H. Cai, T. Taniguchi, K. Watanabe, H. Carrere, D. Lagarde, M. Manca, T. Amand, P. Renucci, S. Tongay, X. Marie, and B. Urbaszek, *Phys. Rev. X* **7**, 021026 (2017).
- [39] Y. Ye, X. Dou, K. Ding, Y. Chen, D. Jiang, F. Yang, and B. Sun, *Phys. Rev. B* **95**, 245313 (2017).
- [40] J. Jadczyk, J. K. Girzycka, P. Kapuściński, Y. S. Huang, A. Wójs, and L. Bryja, *Nanotechnology* **28**, 395702 (2017).
- [41] A. M. Jones, H. Yu, N. J. Ghimire, S. Wu, G. Aivazian, J. S. Ross, B. Zhao, J. Yan, D. G. Mandrus, D. Xiao, W. Yao, and X. Xu, *Nat. Nanotechnol.* **8**, 634 (2013).
- [42] Z. Wang, L. Zhao, K. F. Mak, and J. Shan, *Nano Lett.* **17**, 740 (2017).
- [43] J. Shang, X. Shen, C. Cong, N. Peimyoo, B. Cao, M. Eginligil, and T. Yu, *ACS Nano* **9**, 647 (2015).
- [44] M. Koperski, M. R. Molas, A. Arora, K. Nogajewski, A. O. Slobodeniuk, C. Faugeras, and M. Potemski, *Nanophotonics* **6**, 1289 (2017).
- [45] G. Plechinger, P. Nagler, J. Kraus, N. Paradiso, C. Strunk, C. Schüller, and T. Korn, *Phys. Status Solidi RRL* **9**, 457 (2015).
- [46] G. Plechinger, P. Nagler, A. Arora, R. Schmidt, A. Chernikov, A. G. del Aguila, P. C. M. Christianen, R. Bratschitsch, C. Schüller, and T. Korn, *Nat. Commun.* **7**, 12715 (2016).
- [47] D. Van Tuan, B. Scharf, I. Žutić, and H. Dery, *Phys. Rev. X* **7**, 041040 (2017).
- [48] J. Lindlau, C. Robert, V. Funk, J. Förste, M. Förg, L. Colombier, A. Neumann, E. Courtade, S. Shree, T. Taniguchi, K. Watanabe, M. M. Glazov, X. Marie, B. Urbaszek, and A. Högele, [arXiv:1710.00988v2](https://arxiv.org/abs/1710.00988v2).
- [49] T. Jakubczyk, V. Delmonte, M. Koperski, K. Nogajewski, C. Faugeras, W. Langbein, M. Potemski, and J. Kasprzak, *Nano Lett* **16**, 5333 (2016).
- [50] D. Vaclavkova, J. Wyzula, K. Nogajewski, M. Bartos, A. O. Slobodeniuk, C. Faugeras, M. Potemski, and M. R. Molas, *Nanotechnology* **29**, 325705 (2018).
- [51] F. Cadiz, C. Robert, G. Wang, W. Kong, X. Fan, M. Blei, D. Lagarde, M. Gay, M. Manca, T. Taniguchi, K. Watanabe, T. Amand, X. Marie, P. Renucci, S. Tongay, and B. Urbaszek, *2D Mater.* **3**, 045008 (2016).
- [52] J. P. Echeverry, B. Urbaszek, T. Amand, X. Marie, and I. C. Gerber, *Phys. Rev. B* **93**, 121107(R) (2016).
- [53] M. R. Molas, C. Faugeras, A. O. Slobodeniuk, K. Nogajewski, M. Bartos, D. M. Basko, and M. Potemski, *2D Mater.* **4**, 021003 (2017).
- [54] G. Wang, C. Robert, M. M. Glazov, F. Cadiz, E. Courtade, T. Amand, D. Lagarde, T. Taniguchi, K. Watanabe, B. Urbaszek, and X. Marie, *Phys. Rev. Lett* **119**, 047401 (2017).
- [55] E. Courtade, M. Semina, M. Manca, M. M. Glazov, C. Robert, F. Cadiz, G. Wang, T. Taniguchi, K. Watanabe, M. Pierre, W. Escoffier, E. L. Ivchenko, P. Renucci, X. Marie, T. Amand, and B. Urbaszek, *Phys. Rev. B* **96**, 085302 (2017).
- [56] D. Van Tuan, M. Yang, and H. Dery, *Phys. Rev. B* **98**, 125308 (2018).
- [57] Z. Lin, B. R. Carvalho, E. Kahn, R. Lv, R. Rao, H. Terrones, M. A. Pimenta, and M. Terrones, *2D Mater.* **3**, 022002 (2016).
- [58] A. Singh, G. Moody, K. Tran, M. E. Scott, V. Overbeck, G. Berghäuser, J. Schaibley, E. J. Seifert, D. Pleskot, N. M. Gabor, J. Yan, D. G. Mandrus, M. Richter, E. Malic, X. Xu, and X. Li, *Phys. Rev. B* **93**, 041401 (2016).
- [59] P. K. Chow, R. B. Jacobs-Gedrim, J. Gao, T. Ming Lu, B. Yu, H. Terrones, and N. Koratkar, *ACS Nano* **9**, 1520 (2015).
- [60] M. M. Glazov, T. Amand, X. Marie, D. Lagarde, L. Bouet, and B. Urbaszek, *Phys. Rev. B* **89**, 201302(R) (2014).
- [61] H. Wang, C. Zhang, W. Chan, C. Manolatu, S. Tiwari, and F. Rana, *Phys. Rev. B* **93**, 045407 (2016).
- [62] D. Lagarde, L. Bouet, X. Marie, C. R. Zhu, B. L. Liu, T. Amand, P. H. Tan, and B. Urbaszek, *Phys. Rev. Lett.* **112**, 047401 (2014).
- [63] C. Zhang, H. Wang, W. Chan, C. Manolatu, and F. Rana, *Phys. Rev. B* **89**, 205436 (2014).
- [64] C. Robert, D. Lagarde, F. Cadiz, G. Wang, B. Lassagne, T. Amand, A. Balocchi, P. Renucci, S. Tongay, B. Urbaszek, and X. Marie, *Phys. Rev. B* **93**, 205423 (2016).
- [65] M. Palumbo, M. Bernardi, and J. C. Grossman, *Nano Lett.* **15**, 2794 (2015).

- [66] Q. Cui, F. Ceballos, N. Kumar, and H. Zhao, *ACS Nano* **8**, 2970 (2014).
- [67] M. M. Glazov, E. L. Ivchenko, G. Wang, T. Amand, X. Marie, B. Urbaszek, and B. L. Liu, *Phys. Status Solidi B* **252**, 2349 (2015).
- [68] H. Shi, R. Yan, S. Bertolazzi, J. Brivio, B. Gao, A. Kis, D. Jena, H. Grace Xing, and L. Huang, *ACS Nano* **7**, 1072 (2013).
- [69] A. Hichri, I. Ben Amara, S. Ayari, and S. Jaziri, *J. Phys.: Condens. Matt* **29**, 435305 (2017).
- [70] N. S. Rytova, *Moscow University Physics Bulletin* **22**, 18 (1967).
- [71] A. Chernikov, T. C. Berkelbach, H. M. Hill, A. Rigosi, Y. Li, O. B. Aslan, D. R. Reichman, M. S. Hybertsen, and T. F. Heinz, *Phys. Rev. Lett* **113**, 076802 (2014).
- [72] L. V. Keldysh, *Pis'ma Zh. Eksp. Teor. Fiz.* **29**, 716 (1979) [*JETP Lett.* **29**, 658 (1979)].
- [73] P. Cudazzo, I. V. Tokatly, and A. Rubio, *Phys. Rev. B* **84**, 085406 (2011).
- [74] T. Olsen, S. Latini, F. Rasmussen, and K. S. Thygesen, *Phys. Rev. Lett.* **116**, 056401 (2016).
- [75] A. Hichri, I. Ben Amara, S. Ayari, and S. Jaziri, *J. Appl. Phys.* **121**, 235702 (2017).
- [76] V. Savona and R. Zimmermann, *Phys. Rev. B* **60**, 4928 (1999).
- [77] V. Savona, *J. Phys.: Condens. Matt* **19**, 295208 (2007).
- [78] R. Zimmermann, E. Runge, and V. Savona, *Theory of Resonant Secondary Emission: Rayleigh Scattering Versus Luminescence Quantum Coherence, Correlation, and Decoherence in Semiconductor Nanostructures*, edited by T. Takagahara (Academic, 2003, Kyoto, Japan), p. 89.
- [79] A. O. Slobodeniuk and D. M. Basko, *Phys. Rev. B* **94**, 205423 (2016).
- [80] G. L. Bir and G. E. Pikus, *Symmetry and Strain-Induced Effects in Semiconductors* (Wiley, New York, 1974).
- [81] G. F. Koster, J. O. Dimmock, G. Wheeler, and R. G. Satz, *Properties of Thirty-Two Point Groups* (M. I. T. Press, Cambridge, 1963).
- [82] F. A. Rasmussen and K. S. Thygesen, *J. Phys. Chem. C* **119**, 13169 (2015).
- [83] V. Savona and W. Langbein, *Phys. Rev. B* **74**, 075311 (2006).
- [84] J. Hegarty L. Goldner and M. D. Sturge, *Phys. Rev. B* **30**, 7346(R) (1984).
- [85] C. Robert, M. A. Semina, F. Cadiz, M. Manca, E. Courtade, T. Taniguchi, K. Watanabe, H. Cai, S. Tongay, B. Lassagne, P. Renucci, T. Amand, X. Marie, M. M. Glazov, and B. Urbaszek, *Phys. Rev. Mater.* **2**, 011001(R) (2018).
- [86] F. Cadiz, C. Robert, E. Courtade, M. Manca, L. Martinelli, T. Taniguchi, K. Watanabe, T. Amand, A. C. H. Rowe, D. Paget, B. Urbaszek, and X. Marie, *Appl. Phys. Lett.* **112**, 152106 (2018).
- [87] Note that, unlike in Ref. [6], the numbering of the localized states is done here with ascending order in energy.